



HAL
open science

Hydrothermal genesis and growth of the banded agates from the Allumiere-Tolfa volcanic district (Latium, Italy)

Alessandra Conte, Giancarlo Della Ventura, Benjamin Rondeau, Martina Romani, Mariangela Cestelli Guidi, Carole La, Camilla Napoleoni, Federico Lucci

► To cite this version:

Alessandra Conte, Giancarlo Della Ventura, Benjamin Rondeau, Martina Romani, Mariangela Cestelli Guidi, et al.. Hydrothermal genesis and growth of the banded agates from the Allumiere-Tolfa volcanic district (Latium, Italy). *Physics and Chemistry of Minerals*, 2022, 49, 339, p. 22-34. 10.1007/s00269-022-01214-5 . insu-03869096

HAL Id: insu-03869096

<https://insu.hal.science/insu-03869096>

Submitted on 24 Nov 2022

HAL is a multi-disciplinary open access archive for the deposit and dissemination of scientific research documents, whether they are published or not. The documents may come from teaching and research institutions in France or abroad, or from public or private research centers.

L'archive ouverte pluridisciplinaire **HAL**, est destinée au dépôt et à la diffusion de documents scientifiques de niveau recherche, publiés ou non, émanant des établissements d'enseignement et de recherche français ou étrangers, des laboratoires publics ou privés.



Distributed under a Creative Commons Attribution 4.0 International License



Hydrothermal genesis and growth of the banded agates from the Allumiere-Tolfa volcanic district (Latium, Italy)

Alessandra Conte^{1,4} · Giancarlo Della Ventura^{1,2,3} · Benjamin Rondeau⁴ · Martina Romani² · Mariangela Cestelli Guidi² · Carole La⁴ · Camilla Napoleoni¹ · Federico Lucci⁵

Received: 19 April 2022 / Accepted: 22 August 2022 / Published online: 28 September 2022
© The Author(s) 2022

Abstract

In this work, we studied the hydrothermal agates from the Neogene–Quaternary volcanic district of Allumiere-Tolfa, north-west of Rome (Latium, Italy) using a combination of micro-textural, spectroscopic, and geochemical data. The examined sample consists of (1) an outer cristobalite layer deposited during the early stages of growth, (2) a sequence of chalcedonic bands (including i.e., length-fast, zebraic, and minor length-slow chalcedony) with variable moganite content (up to ca. 48 wt%), (3) an inner layer of terminated hyaline quartz crystals. The textures of the various SiO₂ phases and their trace element content (Al, Li, B, Ti, Ga, Ge, As), as well as the presence of mineral inclusions (i.e., Fe-oxides and sulfates), is the result of physicochemical fluctuations of SiO₂-bearing fluids. Positive correlation between Al and Li, low Al/Li ratio, and low Ti in hyaline quartz points to low-temperature hydrothermal environment. Local enrichment of B and As in chalcedony-rich layers are attributed to pH fluctuations. Analysis of the FT-IR spectra in the principal OH-stretching region (2750–3750 cm⁻¹) shows that the silanol and molecular water signals are directly proportional. Strikingly, combined Raman and FT-IR spectroscopy on the chalcedonic bands reveals an anticorrelation between the moganite content and total water (SiOH + molH₂O) signal. The moganite content is compatible with magmatic-hydrothermal sulfate/alkaline fluids at a temperature of 100–200 °C, whereas the boron-rich chalcedony can be favored by neutral/acidic conditions. The final Bambauer quartz growth lamellae testifies diluted SiO₂-bearing solutions at lower temperature. These findings suggest a genetic scenario dominated by pH fluctuations in the circulating hydrothermal fluid.

Keywords Agate genesis · Moganite · FT-IR and Raman mapping · Hydrothermal fluids · Water behavior in silica · LA-ICP-MS geochemistry

Introduction

Agate is an aesthetically valuable material consisting of a layered sequence of microcrystalline and fibrous quartz intermixed with other silica phases such as moganite, cristobalite, and/or opal depending on the age of silica mineralization and its formation conditions (i.e., pH and temperature). It often fills cavities and veins in volcanic or sedimentary rocks (Dumańska-Słowik et al. 2018; Götze et al. 2020; Pršek et al. 2020) where silica deposition is triggered by post-magmatic hydrothermal activity, combined with the influx of meteoric waters. Notably, the names used in literature for the microcrystalline varieties of silica are numerous and often used in distinct meanings, rendering reading sometimes confusing. In this study, we use the terms with the following meanings: quartz, moganite and cristobalite represent different silica

✉ Alessandra Conte
alessandra.conte@uniroma3.it

¹ Dipartimento di Scienze, Università di Roma Tre, L. S. Leonardo Murialdo 1, 00146 Rome, Italy

² INFN-Laboratori Nazionali di Frascati, Via E. Fermi 54, Frascati, 00044 Rome, Italy

³ INGV, Via di Vigna Murata 605, 00143 Rome, Italy

⁴ Laboratoire de Planétologie et Géosciences, Université de Nantes, 2 rue de la Houssinière, BP 92208, 44322 Nantes, France

⁵ Dipartimento di Scienze della Terra e Geoambientali, Università degli Studi di Bari Aldo Moro, Via E. Orabona 4, 70125 Bari, Italy

polymorphs that can be distinguished on the basis of X-ray diffraction (XRD) and Raman spectroscopy. Chalcedony is a type of α -quartz consisting of microcrystalline fibers that are polysynthetically twinned according to the Brazil law (Miehe et al. 1984; Cady et al. 1998; Heaney 1993). Chalcedony can be furtherly divided into length-slow (also called quartzine, with the optical axis parallel to the fibers; Michel-Lévy and Munier-Chalmas 1892; Flörke et al. 1991), length-fast (also called chalcedonite, with the optical axis perpendicular to the fibers elongation; Folk and Pittman 1971) and zebraic (length-fast with helical twisting of fibers along the c -axis). All of these varieties still have the α -quartz arrangement (hexagonal symmetry) from a structural point of view. Moganite is instead a silica polymorph with monoclinic symmetry that consists of an alternate stacking of layers of right- and left-handed quartz, i.e., periodic Brazil twinning on the unit cell scale (Miehe and Graetsch 1992). Pure moganite samples have been documented only from Gran Canaria (Flörke et al. 1976, 1984) but a certain amount of moganite commonly occurs intergrown with chalcedony across the agate layers (Graetsch et al. 1987; Heaney and Post 1992; Natkaniec-Nowak et al. 2016; Dumańska-Słowik et al. 2018). Overall, length-slow chalcedony and moganite form in alkaline or sulfate environments at high pH conditions (Kastner 1980; Heaney et al. 1992), while length-fast (“normal”) chalcedony is common in non-sulfate environments at neutral to acid pH (Folk and Pittman 1971), although the exact controls of their formation are still poorly understood (Keene 1983).

These silica phases are also typically associated with other minerals such as Fe-oxides, sulfates, carbonates, as well as carbonaceous material whose presence may provide information about the complex processes of agate formation (Richter et al. 2015; Dumańska-Słowik et al. 2018). Opal is also commonly found intermixed with the other silica phases in agate, and is classified into three main categories based on the compact arrangement of their constituent microspheres: opal-A which is totally amorphous, opal-CT, consisting of intermixed cristobalite + tridymite lepispheres and opal-C consisting of cristobalite spheres (Jones and Segnit 1971; Elzea and Rice 1996; Behl 1999; Sodo et al. 2016; Curtis et al. 2019). Opal may be found in both sedimentary and volcanic settings whilst its genesis is always connected to the presence of an aqueous fluid in the geological system (Rondeau et al. 2012; Chauviré et al. 2017). Due to its amorphous and porous structure, opaline silica may trap up to 15 wt% water (both as H_2O and Si-OH silanol groups), located in the voids between the silica sphere or in the form of interstitial films (Thomas et al. 2010; Boboň et al. 2011; Sodo et al. 2016; Chauviré and Thomas 2020); by contrast, microcrystalline silica (i.e., chalcedony and moganite) allows the confinement of

a relatively small amount of water (1–2 wt%) (Flörke et al. 1982; Graetsch et al. 1985; Knauth 1994).

The segregation of the SiO_2 polymorphs, along with their differing compositional and microstructural properties, generates the concentric patterns typically observed in banded agates thus the analysis of the varying amounts of water in the bands can provide a useful tool to determine the mineral species present (Graetsch et al. 1985). Despite several papers that have been devoted to this issue (Graetsch et al. 1985; Heaney 1993; Götze et al. 1998; French et al. 2013; Awadh and Yaseen 2019), the exact mechanism of agate formation is still poorly known. It is generally proposed that agates originate either by precipitation from siliceous fluids or from in situ crystallization from a silica gel. In the first model, hydrothermal siliceous influxes with differing levels of silica saturation and trace element concentrations are thought to precipitate the different silica polymorphs (Lee 2007; Dumańska-Słowik et al. 2013, 2018; French et al. 2013; Natkaniec-Nowak et al. 2020); for example, quartz may precipitate from a relatively low silica concentration, giving rise to few defective crystals (Heaney and Davis 1995). In the second model, silica gel crystallizes in a banded manner by self-organization, and the oscillatory zonation results from a cyclic interplay between growth rate and diffusion rates at a crystal/solution interface (Fron del 1985; Wang and Merino 1990; Merino et al. 1995; Howard and Rabinovitch 2018). The temperature of formation may vary from ambient (weathering) to more than 200 °C (hydrothermal systems) (Götze et al. 2001, 2009, 2020; Moxon and Palyanova 2020).

In this work, we investigated banded agate sample from the Allumiere-Tolfa volcanic district (Latium, Italy) with the aim to define their hydrothermal genesis. There is an extensive although very old literature dealing with the petrography of the igneous rocks in this district (Marinelli 1961; Lauro et al. 1965; Lombardi et al. 1965a, 1965b; Negretti et al. 1966; Taylor and Turi 1976; Vollmer 1977) and to the mineralogy/geochemistry of the ore deposits exploited over the centuries for mining activities (Lombardi and Sheppard 1977; Masi et al. 1980; Calderoni et al. 1985). The silica mineralization widespread in this area, on the contrary, have never been studied. In the Allumiere-Tolfa area, agates are common and are found as veins or as fragments scattered in the field. The sample were studied with a multi-technical approach to document their occurrence and tentatively constrain the agate deposition mechanism by the hydrothermal fluids. We used, in particular, vibrational (FT-IR and Raman) spectroscopies with the aim of assessing the water distribution across the sample and relate its presence with the chalcedony and moganite structural variation.

Study area

The study area (Fig. 1) is located in a transitional sector between the Tuscan and Roman magmatic provinces (De Rita et al. 1997) and was affected by intense volcanic activity spanning from the middle Miocene to the late Pliocene (Serri et al. 1993).

The lava domes that strongly characterize the geomorphology of the area consist of hypo- to holo-crystalline and vitrophyric rhyolites and quartz-latites (Negretti et al. 1966; Lombardi et al. 1974; Cimarelli and De Rita 2006). These volcanic rocks show a porphyritic texture and a fludal fabric consisting of glomerocrysts made up of alkali feldspar + andesine + diopside + quartz in a generally hypohyaline groundmass. The study area was affected by widespread post-volcanic magmatic-hydrothermal activity, which extensively affected the volcanic products as well as a large portion of the underlying sedimentary rocks. Hence fresh and unaltered volcanic rocks are rare because of the late-stage processes, such as illitization of sanidine (Fig. 2a), chloritization of pyroxene (Fig. 2b) and biotite (Fig. 2c), albitization of plagioclase (Fig. 2d) and silica veining (Fig. 2b, d), strongly obliterated the primary assemblages.

The hydrothermal activity gave rise to two distinct areas hosting ore deposits intensively exploited since the Middle Ages up to the last century (Della Ventura and Patanè

2020). The first area is located south of the Allumiere town, within the sedimentary country rocks and mainly consists of Fe-oxide and (Pb, Fe, Cu, Zn, Ag, Hg)-sulfide mineralization (Ferrini et al. 1975; Calderoni et al. 1985). The second area, which is the target of this study (Fig. 1), is located to the north and consists of late-stage hydrothermal alteration products of the volcanic body, mainly alunite and kaolinite, possibly combining both hydrothermal alteration and weathering (Lombardi and Sheppard 1977). The hydrothermal event giving rise to the sulfate and argillitic deposits is also associated with a pervasive deposition, within the volcanic rocks, of opaline and/or microcrystalline silica, consisting of mineral replacements, veins and agate druses (Fig. 2e, f). Although the sulfide-sulfate and argillitic products were studied in the second half of the last century (Lombardi and Sheppard 1977), the silica mineralization is still unaddressed. Investigations of the texture, genesis, and significance of these agate occurrences is the aim of this work.

Materials and methods

Several opaline samples scattered in the Allumiere-Tolfa area were the subject of a master's thesis at the University of Roma Tre; we focus this paper on one agate sample from a vein close to Monte Rovello (Fig. 1). We prepared several slices of various thickness depending on the

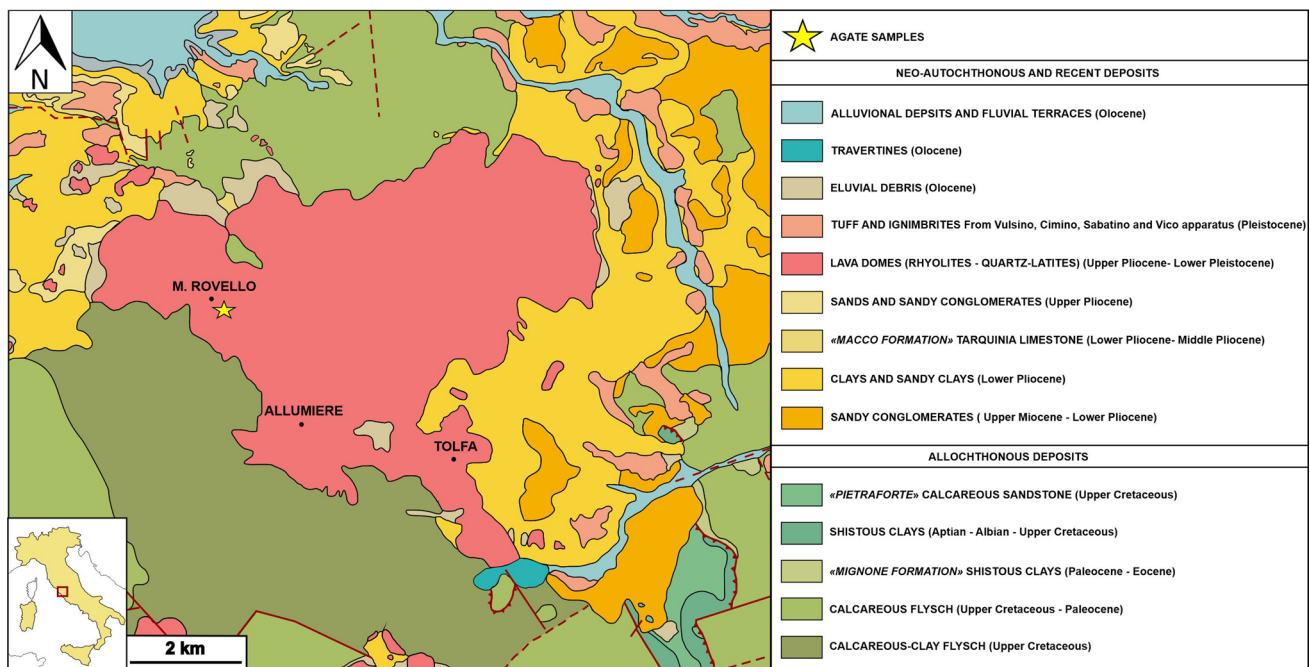


Fig. 1 Geological map of the Allumiere-Tolfa volcanic district (Lazio, Central Italy), modified after Fazzini et al. (1972). The agate ample was collected in the M. Rovello area (Lava domes unit consist of rhyolites and quartz-latites rocks)

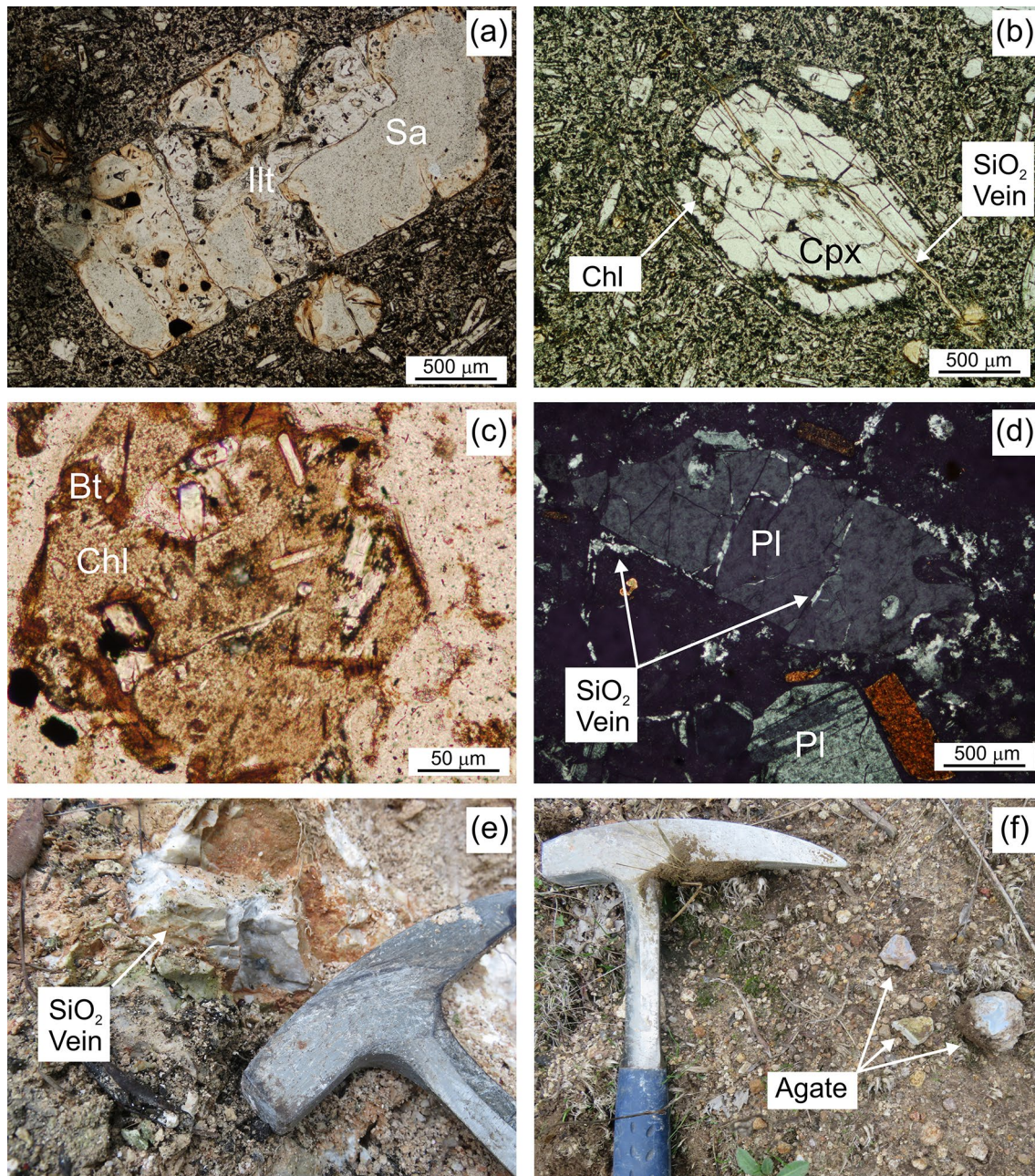


Fig. 2 Field observations and petrography. **a–d** Thin section images of the agate-hosting hydrothermalized quartz-latitude lava: **a** illitization (Illt) processes on sanidine (Sa) phenocryst, **b** chloritization (Chl) of a clinopyroxene (Cpx) crosscut by a silica vein, **c** chloritization (Chl)

of a biotite (Bt) phenocryst, and **d** albitized plagioclases (Pl) also affected by diffuse SiO₂ micro-veins. **e, f** Representative field images showing the occurrence and spatial relation between the agates and the hosting volcanic rocks

analytical methods used. One 200 μm section was used for standard petrographic investigation on the texture of the layers, SEM investigation, and IR and Raman spectroscopy. An additional 30 μm thin section was prepared for specific distinction between length-slow and length-fast chalcedony fibers.

Optical microscopy

The agate thin section was examined under polarized light microscopy with the use of a Nikon Eclipse 50iPol polarized-light microscope (PLM, Nikon, Tokyo, Japan) equipped with a Nikon Ds-Fi2 CCD camera (Nikon, Tokyo, Japan).

Images were acquired using a 10x objective and the Nikon Nis-Elements software (Ver4.30.01, Nikon, Tokyo, Japan). We also used a Keyence VHX2000 numerical microscope to acquire larger images under High Dynamic Range (HDR) mode to enhance the contrast of the pictures. Both transmitted and reflected light were used, under 200x to 500x magnification.

Scanning electron microscopy (SEM–EDX)

SEM investigation was carried out on carbon-coated polished sections using a 7600 JEOL SEM at Institut des Matériaux Jean Rouxel de Nantes (University of Nantes, France). The system was operated at 15 kV accelerating voltage and 0.5 nA current, with a working distance of 8 mm. Images were acquired using backscattered electron detector (BSE) and elemental analyses using a high-resolution energy dispersive spectrometer (EDX) equipped with a Bruker silicon drift detector (SDD) X-ray detector.

Raman micro-spectroscopy (RS)

Raman scattering experiments on the silica phases and solid inclusions were done with a Labram HR Evolution Raman Spectrometer equipped with a 532 nm laser at a 150 mW power at the Laboratoire de Planétologie et Géosciences, University of Nantes, France. Spectra were acquired between 300 and 1200 cm^{-1} with 30 s acquisition time and twice accumulation. We used a 1200 grooves/mm diffraction grating and 100x objective lens. The spectrometer calibration was set using the 520.70 cm^{-1} band of a silicon plate as reference. We considered the 0.5 cm^{-1} spectral resolution suitable without requiring apparatus correction. The spectra of sulfate inclusions were recorded using lower laser power (50 mW) to avoid heating effects. The identification of mineral phases was supported by CrystalSleuth software (RRUFF project, <https://rruff.info>). The spectra of the silica phases were background corrected by the user defined mode of the OriginPro 8.5 software (OriginLab, Northampton, Massachusetts, USA). The curve-fitting algorithm in the OriginPro software was used to fit the spectra in the 400–550 cm^{-1} range using two peaks at 502 cm^{-1} of moganite and 464 cm^{-1} of quartz (Götze et al. 1998, 2020, 2021; Dumańska-Słowik et al. 2013, 2018; Natkaniec-Nowak et al. 2016, 2020; Palyanova et al. 2020; Pršek et al. 2020; Zhang et al. 2020). The peak parameters (e.g., position, width, and area) were obtained by fitting the spectra with Lorentzian functions constrained by a constant minimum baseline. We further calculated moganite concentrations based on the calibration curve provided by Götze et al. (1998). The obtained values may be considered with caution as they may differ from those obtained by X-ray diffraction. However the

obtained values are considered for their relative variations along the sample using a single method.

Raman maps to investigate the moganite distribution across the layers of the agate sample were acquired using a Raman Spectrometer NRS-5100 at Italian National Institute of Nuclear Physics (INFN) in Frascati (Italy), equipped with a 532 nm laser. Conditions of measurement were set at a power of 10 mW, 5 s acquisition time and 20 times accumulation, and a 1 cm^{-1} spectral resolution; a total of 704 spectra were recorded with a 45 μm step. The distribution of moganite was investigated by integrating the area of the moganite peak at 502 cm^{-1} across the studied area.

Fourier transform infrared micro-spectroscopy (μ -FT-IR)

The μ -FT-IR data were collected on the same free-standing doubly-polished thin section used for Raman work. FT-IR analyses in transmission mode were performed at the DAFNE-Light INFN-LNF Facility, by using a Vertex 70 V spectrometer coupled with a Hyperion 3000 IR microscope (Bruker Optics) and a single element MCT (HgCdTe) detector. A quartz source was used, coupled with a KBr beam-splitter, spectra were collected in the NIR-MIR range (from 6000 to 600 cm^{-1}).

The distribution of water in chalcedony was investigated by integrating the intensity in the 2750–3750 cm^{-1} region. A total of 272 FT-IR spectra were collected by using a $100 \times 100^3 \mu\text{m}$ beam and displacing the sample every 100 μm using a motorized stage (Della Ventura et al. 2014) such as to cover a continuous area. 32 scans were averaged for each spectrum at 4 cm^{-1} nominal resolution. Selected spectra were decomposed using the curve-fitting algorithm of the OriginPro software, in the 2750–3750 cm^{-1} range to discriminate the molecular water bands from the silanol ones. A total of six components were used for the fitting procedure, based on the literature data (Eckert et al. 2015; Anedda et al. 2003; Davis and Tomozawa 1996; Aines and Rossman 1984; Langer and Flörke 1974) and the experimental evidence.

Laser ablation inductively coupled plasma mass spectrometer (LA-ICP-MS)

LA-ICP-MS data were acquired by using a quadrupole ICP-MS Varian 820-MS, coupled with a 193 nm excimer laser ablation system (Analyte G2, Photon Machine), at the Laboratory of Planetology and Geodynamics (LPG in Nantes University, France). We used the single-point analysis mode and monitored simultaneously the following nine isotopes: ^7Li , ^{11}B , ^{27}Al , $^{47,49}\text{Ti}$, ^{71}Ga , $^{72,73}\text{Ge}$, ^{75}As . This choice was done to exclude isobaric interferences of isotopes from other elements. The chosen parameters of acquisition were 65 to

50 μm of spot diameter, scan speed of 5 $\mu\text{m}/\text{s}$ for a replicate time of 120 s (60 s of sampling time, 30 s before and after for blank), 10 Hz laser pulse repetition rate, and a fluence of 3.63 J/cm^2 (energy set point of 4 mJ, laser output 60%). Helium was used as a gas carrier of the ablated material, and the sample is pre-ablated to avoid surface contamination as much as possible. Calibration was done using two NIST (National Institute of Standards and Technology, USA) 610 and 612 glasses. Recommended values for these reference materials can be found in Jochum et al. (2011). All elemental concentrations were calculated relative to the ^{29}Si isotope, chosen as internal standard with an assumed concentration of 99.5%. Precision is estimated to be $> 5\%$.

Results

Macro and microscopic observation

Agates from the Allumiere-Tolfa area usually occur as small specimens of wall-lining (“fortification”) silica, both as hydrothermal veins and as fragments scattered in the fields varying in sizes up to several centimeters in dimension. The sample (Fig. 3a) consist of rhythmic layers that exhibit

alternating white-colored and translucent zones which vary in thickness up to ~ 0.5 mm. In reflected light the layers appear to be white and grey (Fig. 3b), corresponding to brown and whitish colors, respectively, observed in transmitted light (Fig. 3c). The outermost layer (#1 in Fig. 3c), at the contact with the host rock, is rich in spherulitic structures that, however, are well resolved only at SEM magnifications and will be described below. This layer is followed by a sequence of crypto-crystalline to fibrous chalcedony (layers #2–9 in Fig. 3c). The individual chalcedonic bands present sharp and re-entrant angles typical of the so-called colloform habit (Fig. 4a). The last layer of the sequence (#11 in Fig. 3c), consist of the last generation of silica, and shows macrocrystalline prismatic quartz crystals up to 200 μm in diameter. The boundaries between the layers are mostly smooth, except for two nucleation layers (#5 and 7 in Fig. 3c) that display a sharp contact with the preceding layer (Figs. 3c, 4b). Microscopic investigations revealed that chalcedony shows differing grain sizes and morphology (from granular to fibrous) and occurs both as common length-fast “normal” and length-slow chalcedony (varieties). In more detail, length-fast chalcedony is more abundant and occurs intermixed with various amounts of length-slow chalcedony across the layers. Moreover, length-fast chalcedony

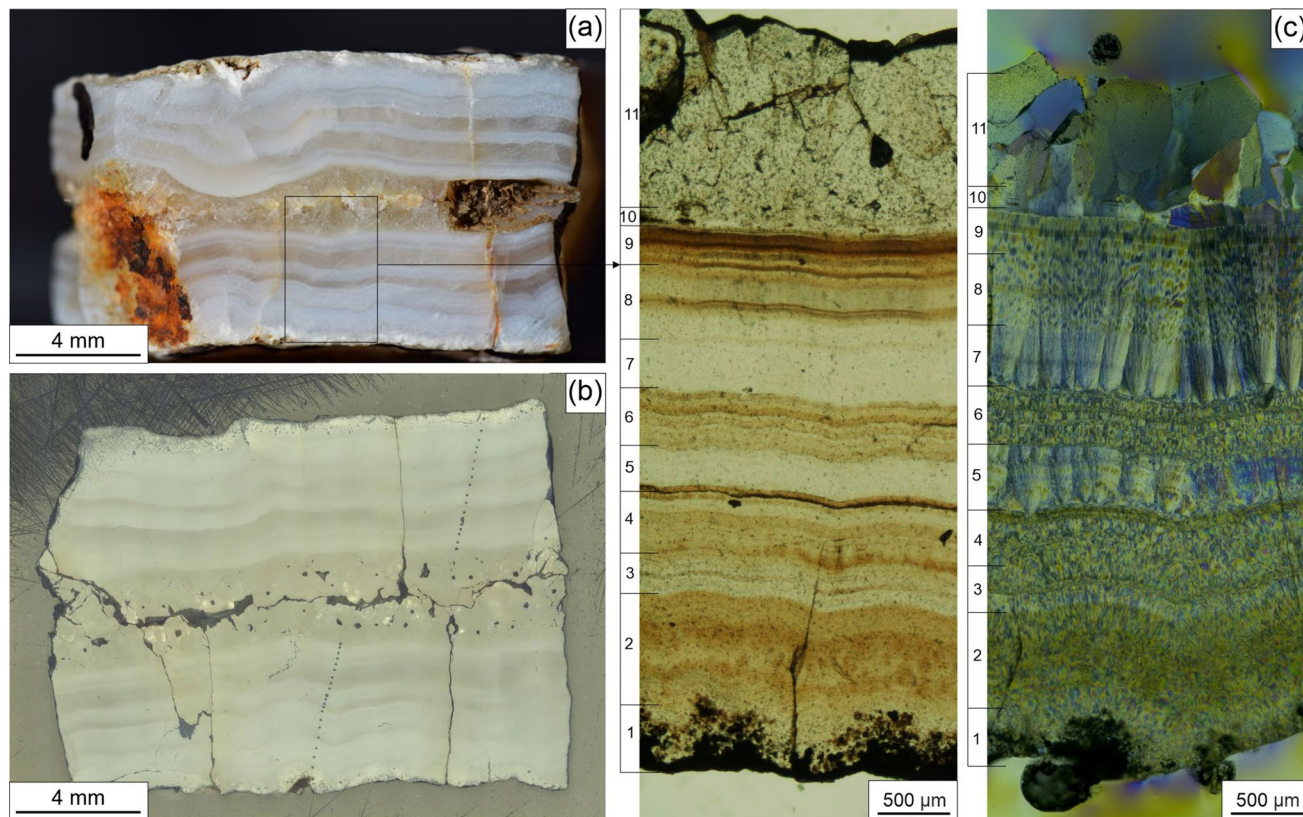


Fig. 3 Wall-lining agate sample occurring as a hydrothermal vein. **a** Macroscopic appearance, of the sample **b** as seen in reflected light; **c** transmitted light image with parallel (left) and crossed (right) polarizers

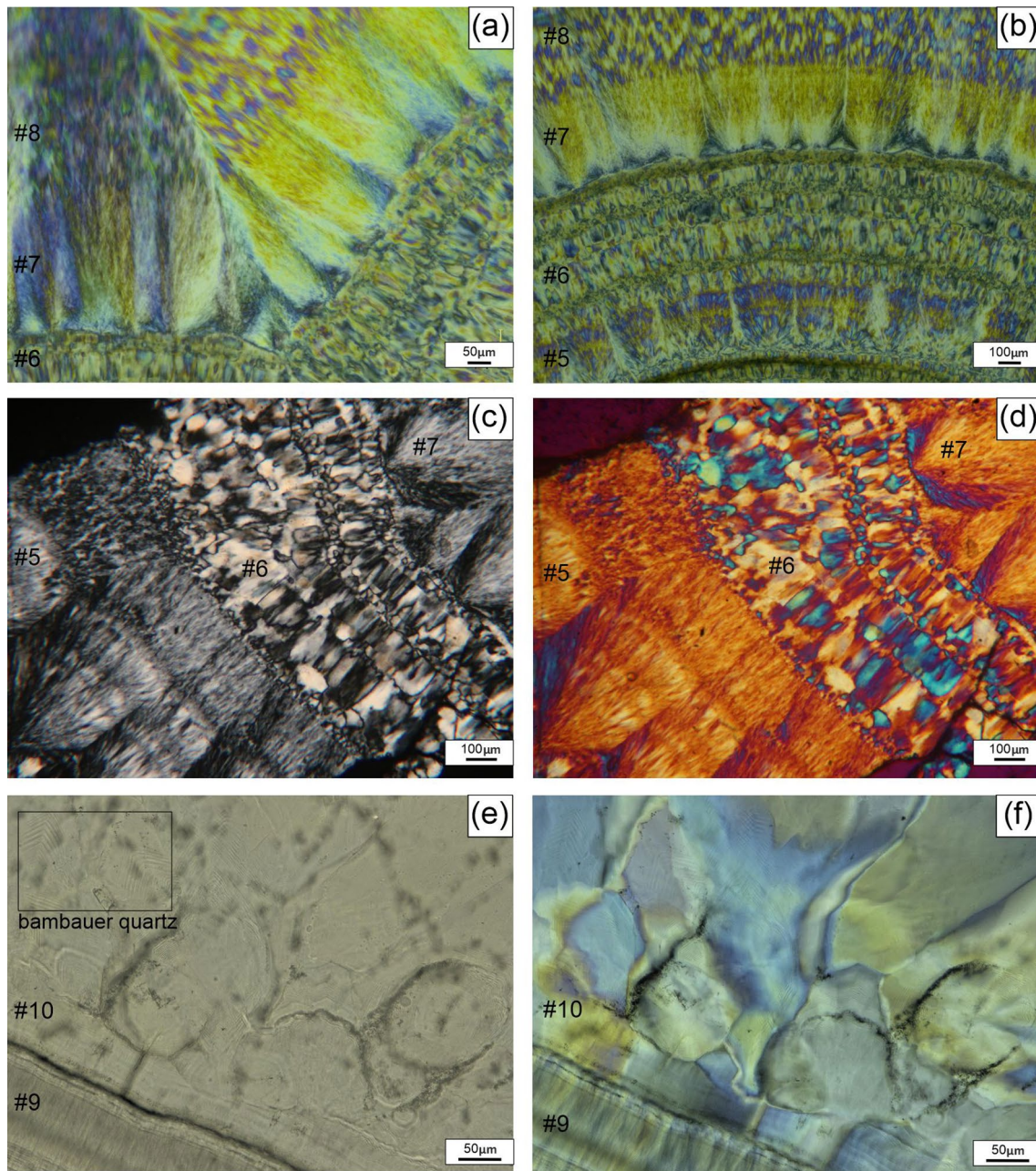


Fig. 4 **a** Colloform appearance; crossed polarizers; **b** nucleation layers (#5 and 7) displaying a sharp contact of the boundary. The second nucleation layer (#7) propagates with fibers elongating from the nucleation point to the layer #8 which consist of zebraic chalcidony; crossed polarizers; **c** alternation of thinner and darker length-fast chalcidony fibers of the nucleation layers (#5 and #7) and coarser fibers of intermixed length-fast (dark) and length-slow (light) chalcidony in layer #6; crossed polars on 30 μm thin section; **d**

mixed length slow (bluish) and length fast (yellow-orange) occurring in layer #6; crossed polars with gypsum plate on 30 μm thin section; **e** Bambauer quartz growing lamellae occurring at the contact layer with fibrous chalcidony; parallel polarizers; **f** Smooth transition from fibrous chalcidony to macrocrystalline quartz (layers #9-10-11). In the last stages of growth (#11), quartz occurs as subparallel wall-lining crystals with size increasing towards the core. Quartz crystals display a feathery appearance and granular texture; crossed polarizers

in the two nucleation layers (#5 and 7 in Fig. 3c) occurs as radial and fan-shaped (spherulitic) micro texture with fibers elongated from the nucleation point to the boundary of the layer (Figs. 3c, 4b). As this spherulites join together during growth, to form layers parallel to the cavity wall, this

type of chalcidony is known as “wall-lining chalcidony” (Heaney 1993). The fibrous chalcidony layers exhibit a gradual increase in width and length of the fiber along the individual bands, with coarser fibrils discernable from finer ones due to longer twist periodicity and higher birefringence

(Lee 2007). The fiber length ranges from below the optical resolution to $\sim 800\ \mu\text{m}$ at the end of the layer where the fibers terminate. Under crossed polarizers, the last section of these fibrous bands (layer #8–9 in Fig. 3c) exhibit a rhythmic extinction, resulting in a wrinkle band texture that is diagnostic for the presence of zebraic chalcedony (length-fast with helical twisting of fibers along *c*-axis) (Fig. 4b). Through the use of the gypsum plate, it is possible to highlight the presence of length-slow (bluish) and length-fast (yellow) intergrowths across the layers (Fig. 4d). Length-fast chalcedony is the only phase in the nucleation layers #5 and #7 (Fig. 4d), while the #2, #3, #4 and #6 layers consist of predominant length-fast chalcedony intermixed with minor amounts of length-slow chalcedony. At the core of the agate sample, the transition from fibrous chalcedony to hyaline euhedral quartz crystals is smooth, with the layering still visible at the contact zone (Fig. 4e, f). Quartz is organized as subparallel wall-lining crystals which display an increase in size towards the core (Fig. 4f). A recurrent feature at the chalcedony–quartz contact is the presence of μm -sized lamellae testifying to episodic stages of crystal growth and typical of the so-called Bambauer (Bambauer et al. 1961) quartz (Fig. 4e). Moreover, under crossed polarizers, some crystals at the contact with the chalcedony band locally reveal divergent extinctions resulting in a feathery/splintery appearance (Fig. 4f). The quartz crystals in the last stages of growth instead, are prismatic and display granular texture (Fig. 4f).

We performed a transect of high-resolution images perpendicular to the layers with the aim of clarifying the relationships between the observed optical features described above, with features (micro porosity distribution and brightness variations due to change in composition) visible at the electron microscope scale. The first layer of the sample is characterized by the occurrence of the spherules (Fig. 5a) displaying higher porosity with respect to the silica matrix; according to Raman spectroscopy they consist of cristobalite. The silica matrix in most part of the sample is characterized by a continuous tone of grey and nano to submicron pores homogeneously dispersed, with no preferential orientation, and no variation in contrast between the bands seen in optical microscopy (Fig. 5b). The two nucleation layers (#5 and 7 in Fig. 3c) instead display nearly vertical structures of alternatively brighter and darker bands, corresponding to the growth of the silica fibers starting from the aligned half spherulites (Fig. 5c). Within this zone, pores seem to be constrained inside the darker layers of the vertical structures of the fibers. The zebraic chalcedony zone (#8 in Fig. 3c) that occurs in the second nucleation layer shows bands of alternating dark and bright grey at the micron scale, consistent with layering seen with the optical microscope. Moreover, an additional structure is superimposed nearly perpendicular to the layering: it consists of alternating dark

and bright micrometric bands that build up the silica fibers (Fig. 5d). Within this zone, pores seem, at first sight, to be randomly distributed within the structure. However, careful examination of Fig. 5d reveals that pores are slightly more concentrated within bright layers and aligned parallel to the fibers. Layers #9–10 in Fig. 3c display a remarkable alternation of bright and dark gray tonalities at the micron scale, with distinct and sharp boundaries (Fig. 5e), corresponding to the chalcedony layering observed in optical microscopy. These are similar to the iris bands described by Brewster in the 1800s and Frondel in the 1980s. In this area, the pores tend to be concentrated parallel to the layering, without any systematic relationship between pore abundance and the level of grey of the layers. Finally, the quartz layer (#11 in Fig. 3c) shows a very compact structure with few randomly distributed pores (Fig. 5f). As a conclusion, the SEM transect suggests the occurrence of two different scales of porosity, the first one consisting of nano- to sub-micron pores equally dispersed across the whole sample, and a second one of sub-micrometric dimension, which is alternatively distributed in darker or brighter bands. Therefore, porosity does not seem to be related to the compositional sequence.

Mineral inclusions

SEM-BSE observations revealed the presence of various inclusions dispersed in both the first and in the last layers. At the rim of the agate in contact with the host rock, rod-like structures perpendicular to the contact are observed; these occur as brighter elongated structures as seen with back-scattered electrons (Fig. 6a). These rod-like structures contain small hexagonal quartz crystals ($10\ \mu\text{m}$) and a bright intricate mass of polycrystalline needles $< 1\ \mu\text{m}$ in dimension. The needles are composed of high Al, Fe, Mg and K (Fig. 6a, spectrum 1). Their structure suggests a mix of several mineral phases, as yet unidentified (possibly mica-group species, i.e., celadonite). The rod-like features are also covered by coalescing spheres that seem to constitute the initial stage of the agate growth. These spheres were identified as consisting of cristobalite by Raman spectra with peaks 415, 227, 109, 782 and $1080\ \text{cm}^{-1}$ (Bates 1972) (Figure S1 and Tab. S3). Some of these spherules are characterized by evident signs of dissolution (Fig. 6b). The occurrence and distribution of cristobalite (layer #1 in Fig. 3c) is easily observable also just by PLM due to its characteristic botryoidal appearance (Palyanova et al. 2020) and displays a higher porosity and aluminum content (qualitatively estimated by SEM–EDS) with respect to the silica matrix. The initial stage of the agate growth is also marked by the presence of some iron oxides dispersed along the cristobalite layer. Moreover, we noted dark, elongate needles radiating from the rod-like structures outwards into the silica matrix (Fig. 6a–c).

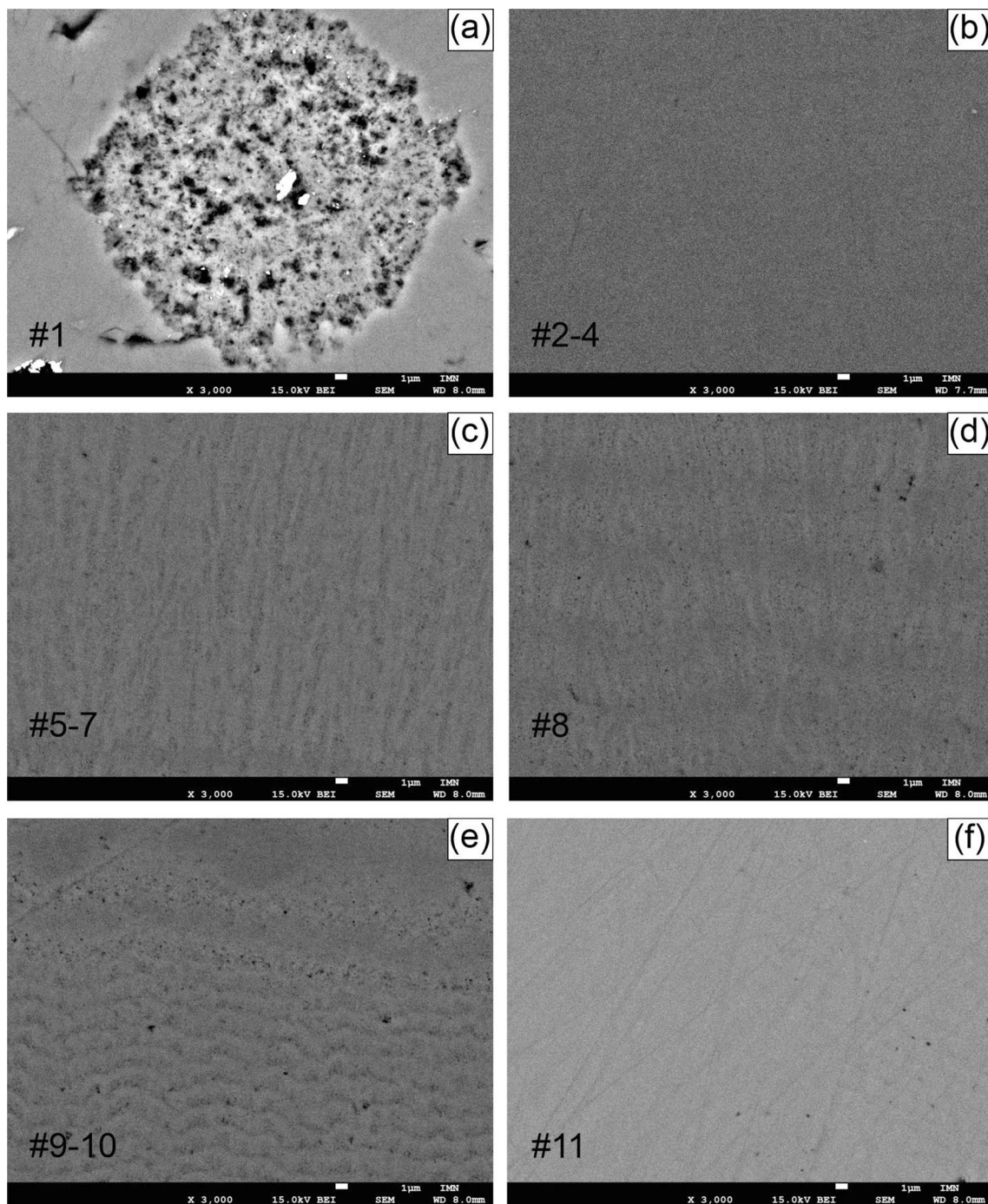


Fig. 5 Back scattered electron (BSE) images across the agate sample. **a** Cristobalite spherules displaying higher porosity with respect to the silica matrix; **b** Homogeneous porosity and grey tone which characterizes most part of the sample, in contrast with the bands seen in optical microscopy; **c** Porosity occurring in vertical structures of silica fibers for the two nucleation layers; **d** Porosity occurring

in brighter bands and distributed vertically in the zebra chalcedony layer; **e** Porosity orientated parallel to bands occurring in lighter and darker bands alternatively, occurring the transition zone from fibrous chalcedony to macrocrystalline quartz; **f** Quartz layer displaying no visible porosity

These needles tend to be hollow when occurring in the porous cristobalite layer and filled in the overlaying, chalcedony layers. EDS measurements reveal high Al content, and minor amounts of Na (Fig. 6, spectrum (2).

Considering that these needles display a BSE grey level darker than surrounding silica, despite their minor content of Ca and K, which are significantly heavier than Si, we hypothesize that they contain significant amounts of light

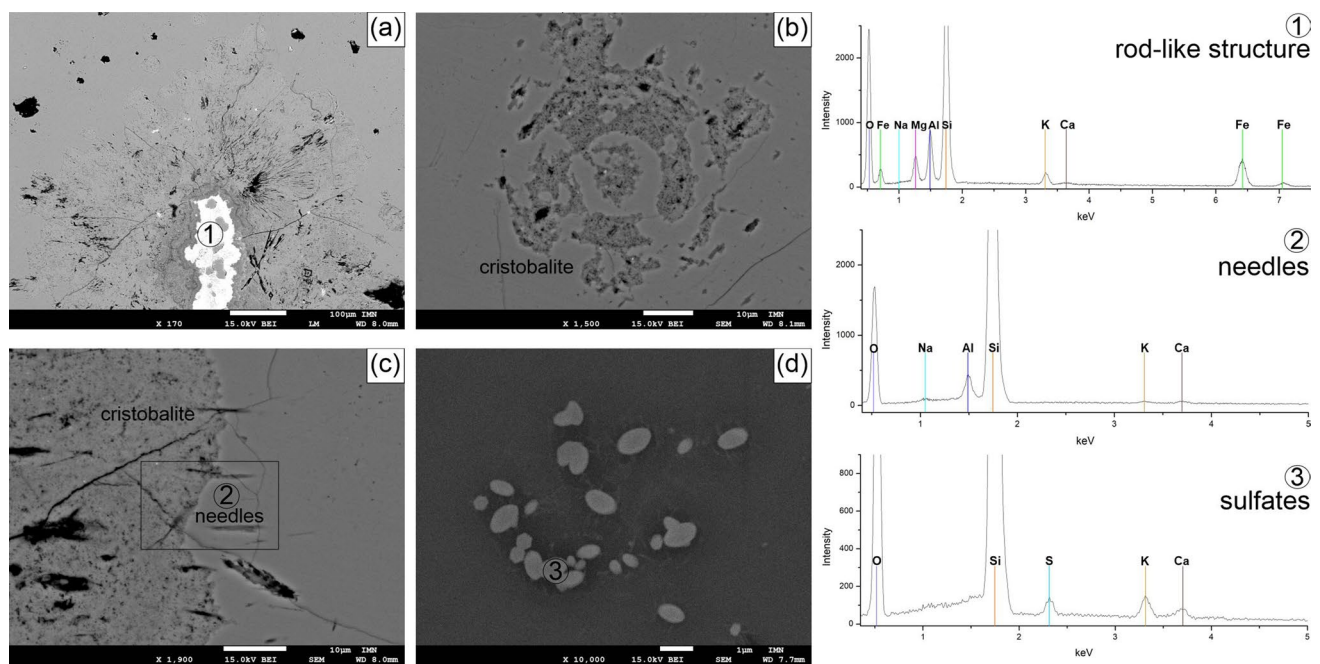


Fig. 6 Back scattered electron (BSE) images of mineral inclusion in the agate sample, occurring in the first and last layer of the growth. **a** Rod-like structure filled bright polycrystalline needles and elongated needles propagating outwards from the rod-like structures into the silica matrix. The rod-like structure is covered by coalescing spheres

of cristobalite which are enlarged in the adjacent image; **b** Spherulitic cristobalite partially dissolved; **c** Hollow and filled needles at the contact between cristobalite and silica matrix; **d** Sulfate inclusions occurring the quartz layer. EDS Spectra of solid inclusions: (1) rod-like structure; (2) needles propagating outwards; (3) sulfates

elements such as hydrogen in the form of water. Finally, the polygonal quartz layer (#11 in Fig. 3c) at the end of the agate crystallization contains numerous sulfate inclusions, as suggested by the 1009 cm^{-1} Raman band (Berenblut et al. 1973) (Figure S2—Tab. S3). These inclusions are elliptical in shape, up to $1\text{ }\mu\text{m}$ in length and frequently occurring in aggregates (Fig. 6d). These sulfates are rich in Ca, Na and K in variable proportions (one example is shown in Fig. 6, spectrum 3), but the chemistry could not be exactly identified because of the small crystal-size. We also observed in the quartz layer very few euhedral aluminosilicates of Fe and Mg of sub-micrometric size.

Vibrational (Raman and FT-IR) micro-spectroscopy

To identify the different silica polymorphs across the sample, we acquired several Raman spectra at different locations across the agate layers. The quantification of the moganite content in chalcedony (in wt. %) is based on the ratio between the Raman band intensity of the Si–O peak at 464 cm^{-1} (attributed to alpha-quartz) and that at 502 cm^{-1} which is assigned to moganite (for more details refer to Götze et al. 1998; Bustillo et al. 2012). Deconvolution parameters are listed in Table 1. A selected example of the spectral deconvolution, along with calculated moganite concentration, is given in Fig. 7a. The spectra collected

Table 1 Fitting parameters for the Raman spectra in the $400\text{--}500\text{ cm}^{-1}$ range

Raman Layer	C1 Peak position (cm^{-1})	C2 Peak position (cm^{-1})	C1 FWHM (cm^{-1})	C2 FWHM (cm^{-1})	C1 Peak height	C2 Peak height	C1 Area intg (arbitrary units)	C2 Area intg (arbitrary units)	Ratio AIntg C2/ AIntg C1	Götze et al. (1998) % Moganite	Adj. R-square
#2	464.09	502.11	9.17	13.49	4304.45	556.30	59498.11	11012.87	0.185	48	9.960
#4	464.14	502.76	8.48	12.07	19125.44	2060.84	243990.78	36647.27	0.150	40	9.965
#6	464.31	502.47	8.34	12.03	19362.51	1103.46	243015.06	19575.87	0.081	30	9.968
#8	464.12	501.67	8.48	12.08	20901.01	1148.35	266575.40	20448.80	0.077	30	9.984
#3	464.18	502.42	7.97	12.85	23110.72	524.35	277526.56	9880.84	0.036	10	9.956
#11	464.37		7.75		23968.78		280639.58			0	9.958

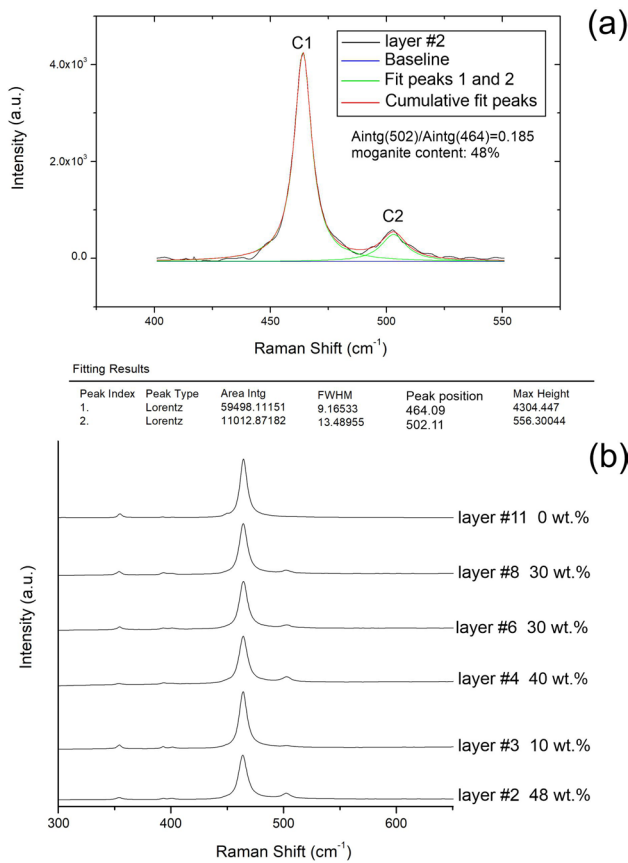


Fig. 7 Selected Raman spectra collected across the layers of the studied agate sample. **a** Example of spectral deconvolution on the spectrum with highest moganite signal; **b** Raman spectra collected in representative sample layers, displaying different moganite contents

along a traverse perpendicular to the layering (Fig. 7b) show that the intensity of the moganite band is zero for the layers corresponding to first and last stages of the agate growth, and has a variable amounts across the sequence of the chalcedony layers. The maximum $I_{(502)}/I_{(464)}$ cm⁻¹ ratio was found in layer #2 at 0.19 (Fig. 7a). Based on the calibration curve proposed by Götze et al. (1998), this ratio corresponds to the moganite content of ca. 48 wt% (for uncertainties, see details in Götze et al. 1998). The minimum 502/464 cm⁻¹ intensity ratio was instead found in layer #3 at 0.04, corresponding to a moganite content of 10%.

FT-IR micro-spectroscopy shows that spectra are similar in shape across the sample and consist of a relatively sharp peak at 3585 cm⁻¹, assigned to the silanol Si–OH groups combined to a broad absorption assigned to H₂O molecules (Iler 1979). The intensity of this signal strongly varies across the samples, revealing a heterogeneous water content (Fig. 8). Water-related band is the most prominent in Layer #3 (Fig. 8). As expected, the spectrum collected in the quartz layer (#11) shows the lowest intensity of the water signal.

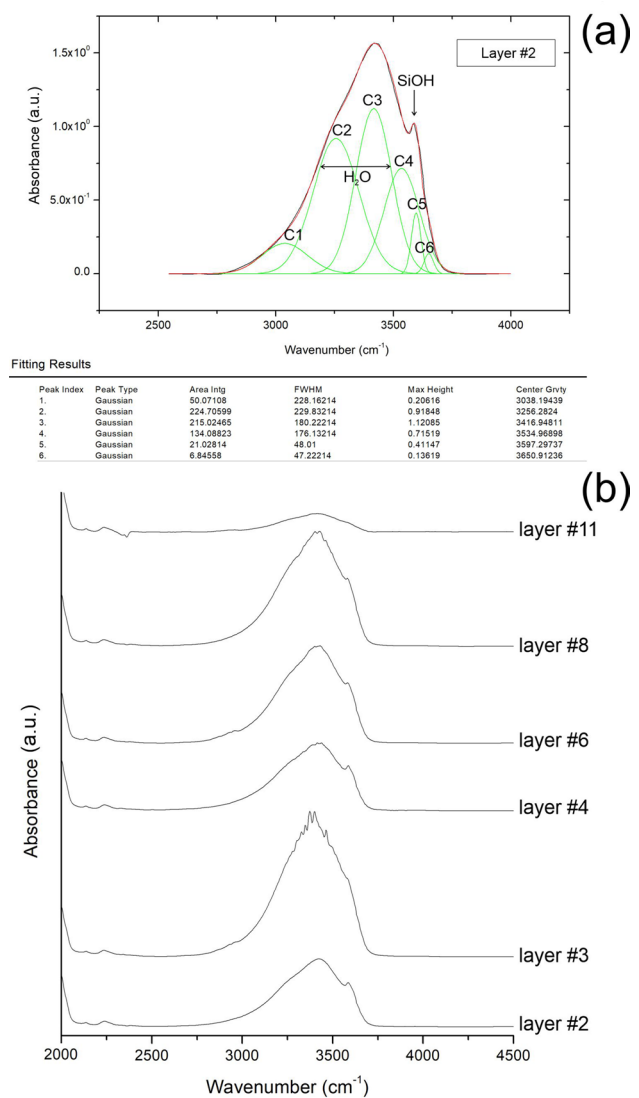


Fig. 8 Selected FT-IR spectra across the layers of the agate sample. **a** Example of spectral deconvolution on the pattern from layer #2. **b** FT-IR spectra in the water stretching region as collected in the different layers, plotted with the same absorbance scale; spectra vertically shifted for clarity

An example of deconvolution on the principal water-stretching region (2750–3750 cm⁻¹) is given in Fig. 8a, for the spectrum from layer #2. The fitting parameters were based on both literature (Langer and Flörke 1974; Aines and Rossman 1984; Flörke et al. 1991; Davis and Tomozawa 1996; Anedda et al. 2003; Day and Jones 2008; Eckert et al. 2015) and experimental evidence. We chose to follow a classification already proposed in literature, defining “Type A” silanols and molecular water the groups that are isolated in the SiO₂ matrix and are not involved in hydrogen bonding; on the other side, “Type B” silanols and molecular water refer to the adsorbed water that resides in relatively large voids with strong hydrogen bonds (Langer and Flörke 1974;

Aines and Rossman 1984; Flörke et al. 1991; Day and Jones 2008). Six components were fitted to each FT-IR spectrum: (i) C1 at $\sim 3040\text{ cm}^{-1}$ ($3038\text{--}3040\text{ cm}^{-1}$), with a FWHM varying from 228 to 265 cm^{-1} . This component is not assigned in literature, although it is obviously related to water; (ii) C2 at $\sim 3260\text{ cm}^{-1}$ ($3256\text{--}3266\text{ cm}^{-1}$), with a FWHM varying from 227 to 240 cm^{-1} . This component is assigned to H-bonded type B molecular water (Davis and Tomozawa 1996), located within the pores of the structure; (iii) C3 at $\sim 3415\text{ cm}^{-1}$ ($3405\text{--}3417\text{ cm}^{-1}$), with a FWHM varying from 175 to 180 cm^{-1} . This component is assigned to type A molecular water, not hydrogen-bonded and located within the silica network (Davis and Tomozawa 1996; Aines and Rossman 1984); (iv) C4 at $\sim 3535\text{ cm}^{-1}$ ($3534\text{--}3536\text{ cm}^{-1}$), with a FWHM varying from 165 to 176 cm^{-1} . This component is assigned to H-bonded type B silanols, located within the pores (Langer and Flörke 1974; Davis and Tomozawa 1996); (v) C5 at $\sim 3560\text{ cm}^{-1}$ ($3597\text{--}3560\text{ cm}^{-1}$), with a FWHM varying from 47 to 48 cm^{-1} . This component is assigned to both type A and type B silanols (Davis and Tomozawa 1996); (vi) C6 at $\sim 3650\text{ cm}^{-1}$, with a FWHM varying from 47 to 49 cm^{-1} . This component refers to non-hydrogen bonded type A silanols, located within the silica structure (Langer and Flörke 1974; Davis and Tomozawa 1996; Eckert et al. 2015). The final fitted parameters and integrated intensities are listed in Table 2.

Inspection of Fig. 9 shows that the silanol signal is directly proportional to the molecular water signal suggesting a coevolution of molecular water and silanols components (Fig. 9a). However it has to be taken into consideration that (i) component C1 was not modeled as it has not been attributed to either SiOH or molH_2O in the literature, and

could possibly change the trend, and (ii) spectra acquired on layer #3 reach total absorption (i.e. the device is not able to detect the real and stronger water signal), and thus the molecular water components modeled during the fitting could be slightly underestimated. Also, Fig. 9b shows that type A and B molecular water components decrease in the same proportion for increasing moganite content, while type B silanols seem to decrease more faster with respect to type A silanols (Fig. 9c). Finally, the intensity of the total absorbance in the $2750\text{--}3750\text{ cm}^{-1}$ range (Fig. 9d) as well as the intensity of the C2-3 components assigned to molecular water (Fig. 9e) and the intensity of the C4-6 components assigned to silanols (Fig. 9f) are all inversely correlated with the moganite content obtained by Raman spectroscopy.

Spectroscopic imaging of moganite and water across the studied agata

The spatial distribution of the moganite across the sample was addressed via Raman imaging; to this purpose, we collected a grid of 22×32 single point spectra and integrated the intensity of the 502 cm^{-1} peak over the scanned areas (Fig. 10a). The resulting image shows that the moganite distribution is roughly uniform within individual chalcedony bands and seems to be concentrated in some discrete layers which appear optically darker in transmitted light (layer #2 and #4 in Fig. 3c). The spatial distribution of H_2O through the agate layers was addressed in a similar way, by collecting a grid of 16×17 single point spectra and by integrating the absorbance in the whole $2750\text{--}3750\text{ cm}^{-1}$ range. The resulting map (Fig. 10b) shows that the water signal (H_2O plus Si-OH groups) is (i) evidently correlated to the layering of

Table 2 Fitting parameters for the FTIR water spectra in the principal OH-stretching ($3750\text{--}2750\text{ cm}^{-1}$) region

FTIR	C1	C2	C3	C4	C5	C6	C1	C2	C3	C4	C5	C6	
Layer	Peak position (cm^{-1})						FWHM (cm^{-1})						% Moganite (Götze et al. 1998)
#2	3038.19	3256.28	3416.95	3534.96	3597.3	3650.91	228.16	229.83	180.22	176.13	48.01	47.22	48
#4	3039.05	3256.06	3416.11	3534.53	3597.01	3650.49	247.74	229.80	180.80	174.81	47.69	49.48	40
#6	3040.39	3258.91	3415.17	3535.84	3597.20	3650.25	265.91	233.07	180.75	176.75	48.74	47.75	30
#8	3039.02	3256.06	3413.54	3536.84	3597.18	3650.18	235.25	229.37	179.37	176.37	48.37	48.37	30
#3	3038.19	3256.67	3405.57	3534.38	3600.03	3650.39	228.73	227.70	180.73	165.69	48.73	47.75	10
#11	3038.86	3266.44	3417.17	3534.98	3597.63	3650.92	228.94	240.54	175.30	169.20	48.95	47.94	0
Layer	Peak height						Area intg (cm^{-1})						Adj. R-square
#2	0.21	0.92	1.12	0.72	0.41	0.14	50.07	224.71	215.03	134.09	21.03	6.84	9.994
#4	0.24	0.91	1.10	0.71	0.42	0.13	62.76	225.04	212.08	132.54	21.12	6.70	9.993
#6	0.28	1.33	1.58	1.06	0.46	0.16	79.06	330.68	303.05	200.20	24.03	8.08	9.992
#8	0.30	1.55	1.89	1.23	0.47	0.16	75.03	380.12	360.08	231.19	24.70	8.03	9.993
#3	0.37	1.89	2.25	1.63	0.46	0.16	90.49	459.53	431.81	287.07	23.80	8.32	9.985
#11	0.04	0.26	0.29	0.19	0.05	0.03	9.94	66.34	54.40	34.54	2.79	1.47	9.985

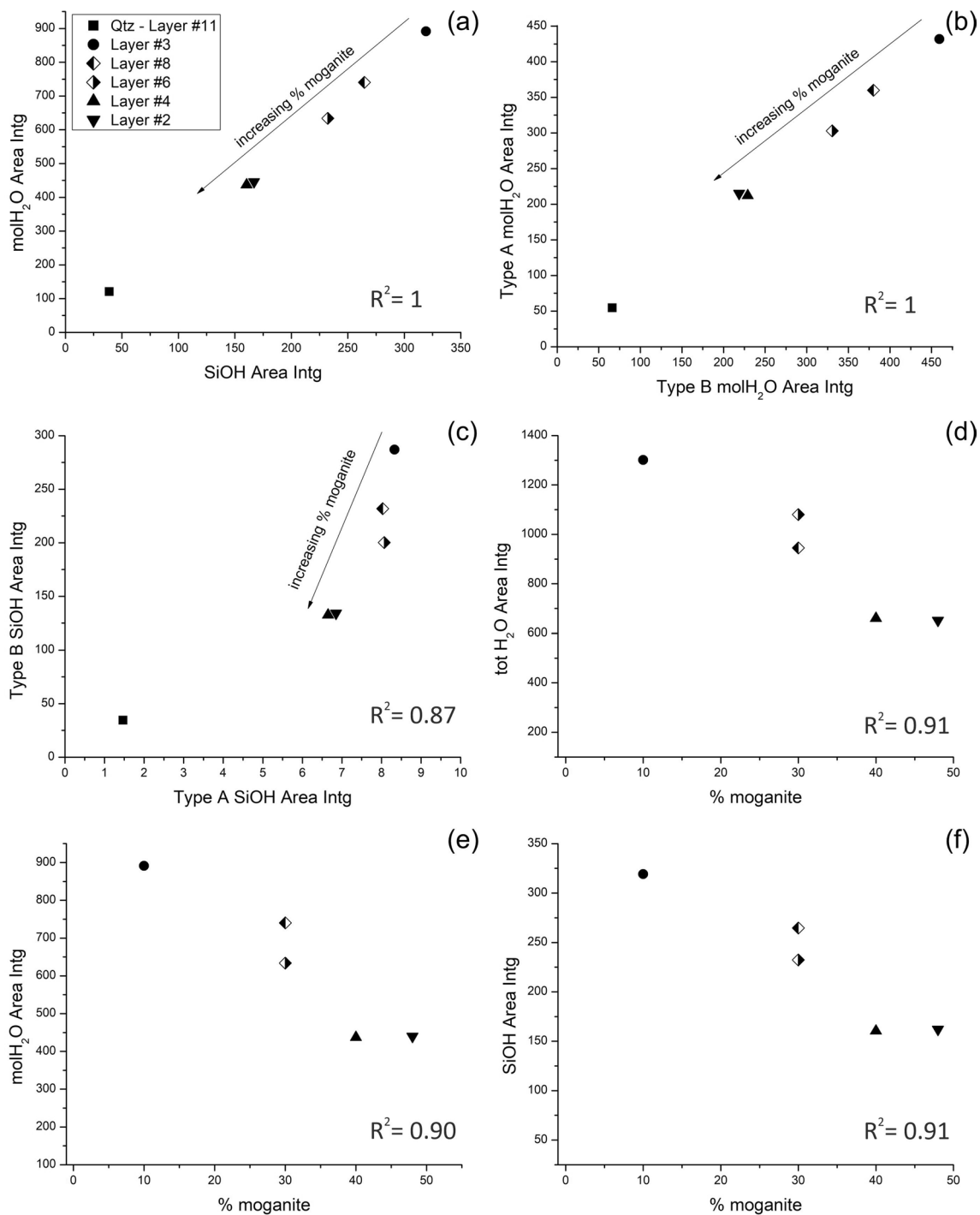


Fig. 9 Plot of integrated intensities of the fitted water components, against the moganite content. R² was calculated excluding the points related to the quartz layer

the agate sample, and (ii) is homogeneous within each layer. Note, however, that while the Raman spectra were collected with a beam-size of 1 μm, the FT-IR data were collected with a beam-size of 200 × 200 μm. This explains the higher homogeneity of the H₂O vs. the moganite distribution within

a single layer, that is apparent when comparing Fig. 10a with Fig. 10b.

Most strikingly, the FT-IR and Raman maps collected in this study visually confirm that there is a clear anticorrelation between the moganite and the water signals. This

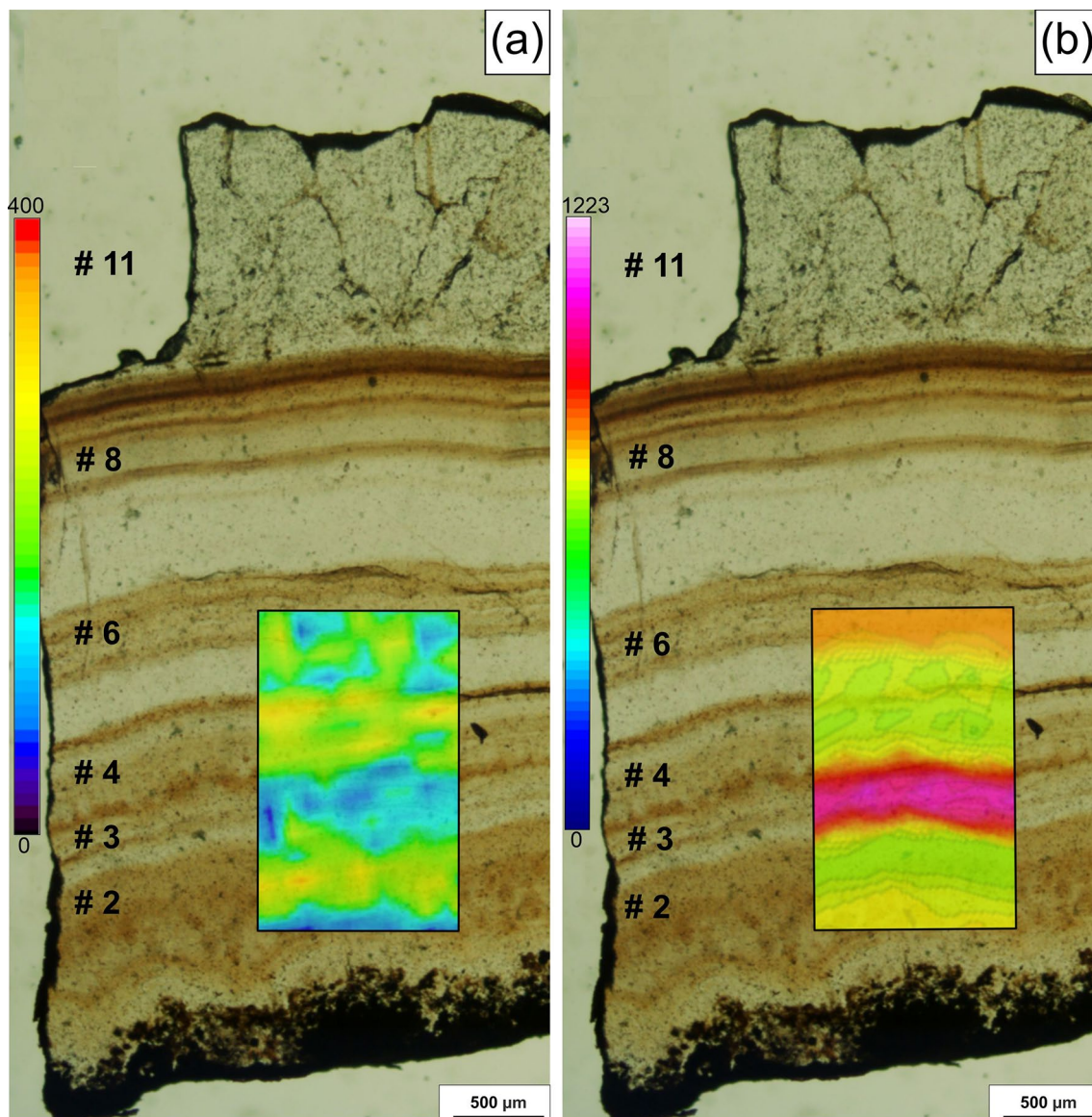


Fig. 10 Comparison between the moganite distribution and the water signal in studied agate. **a** Raman mapping representing spatial distribution of moganite across the layers, calculated based on the integral area of the 502 cm^{-1} peak intensity; **b** FT-IR mapping representing water signal distribution across the layers, calculated based on the

integral area of the $2750\text{--}3750\text{ cm}^{-1}$ principal water band. The color scales for both Raman and FT-IR maps are in arbitrary units, representing the minimum and the maximum values of the integral areas of moganite peak and water band respectively

result is somehow surprising as previous studies suggest the opposite, as detailed in the Discussion section.

Trace elements chemistry

Trace element distribution may be useful in identifying the genetic environment of the studied agate sample (e.g., Müller et al. 2018; Rabiee et al. 2019). We thus collected LA-ICP-MS (laser ablation induced coupled plasma mass spectrometry) data (i) on cristobalite outer rims (#4 spots), (ii) on the main chalcedony-moganite bands (#62 spots

corresponding to #10 spots on moganite-poor layers, #9 spots on moganite-rich layers and #43 spots intermediate moganite content bands) and (iii) on the inner portion consisting of hyaline euhedral quartz crystal (#37 spots). Results are presented in Table 3 and Fig. 11.

The cristobalite outer rims shows low Ti (1.58 ppm, with only one spot higher than the detection limit), high Al (141.00–343.53 ppm) with low Li (1.42–8.12 ppm), high B (22.33–34.91 ppm), Ga (1.31–1.75 ppm), Ge (1.51–3.02 ppm) and As (5.65–9.47 ppm).

Table 3 Trace element geochemistry (ppm) as obtained through in situ LA-ICP-MS analyses of banded agate

	Element (ppm)						
	Ti	Al	Li	B	Ga	Ge	As
Cristobalite outer rim							
<i>n</i> =	1	4	4	4	3	3	4
Average	1.58	226.34	3.54	29.87	1.54	2.28	7.63
Range	n.d	141.00–343.53	1.42–8.12	22.33–34.91	1.31–1.75	1.51–3.02	5.65–9.47
σ_{n-1}	n.d	83.67	3.11	5.29	0.22	0.76	1.56
Chalcedony-moganite layers							
All layers							
<i>n</i> =	12	62	26	62	47	62	61
Average	1.37	83.7	3.38	32.66	0.85	6.53	10.96
Range	0.95–1.94	3.40–302.89	1.18–13.08	7.48–52.86	0.31–2.67	1.18–13.08	1.83–22.73
σ_{n-1}	0.27	75.57	3.12	11.44	0.47	2.82	6.13
Chalcedony layers only							
<i>n</i> =	4	10	6	10	10	10	10
Average	1.13	76.52	3.35	45.64	0.97	8.13	16.51
Range	0.95–1.26	3.44–290.40	1.31–8.27	42.84–49.56	0.44–2.67	4.64–10.20	12.92–19.92
σ_{n-1}	0.15	97.24	2.68	2.44	0.75	1.98	2.18
Moganite layers only							
<i>n</i> =	1	9	6	9	8	9	9
Average	1.24	132.42	2.08	32.93	0.93	2.43	8.69
Range	n.d	13.17–302.89	1.26–4.16	26.94–39.25	0.31–2.14	1.18–3.64	5.49–14.55
σ_{n-1}	n.d	95.95	1.05	4.33	0.6	0.78	2.61
Hyaline quartz inner sector							
<i>n</i> =	5	29	29	26	28	22	26
Average	2.46	88.54	38.24	16.22	1.01	3.42	6.74
Range	1.13–3.95	4.42–295.92	1.41–133.93	3.82–28.99	0.39–1.51	1.70–5.15	2.40–10.30
σ_{n-1}	1.27	81.51	34.63	7.16	0.32	0.87	2.32

The chalcedony–moganite bands show extremely low Ti (0.95–1.94 ppm, with #50 spots having Ti below the detection limit, bdl) and high Al (3.40–302.89 ppm) contents, with local enrichment in Li (1.09–13.59 ppm), B (7.48–52.86 ppm), Ga (0.31–2.67 ppm), Ge (1.18–13.08 ppm) and As (1.83–22.73 ppm).

In particular (Table 3) the chalcedony-rich bands have lower Al than the moganite-richer ones (mean 76.52 ppm vs. 132 ppm) and higher B (mean 45.64 vs. 16.22 ppm), Ge (mean 8.13 vs. 2.43 ppm) and As (mean 16.51 vs. 8.69 ppm).

The hyaline quartz at the core of the banded agate shows low Ti (1.13–3.95 ppm with #32 spots having Ti bdl) and high Al (4.42–295.92 ppm) with a general enrichment in Li (1.41–133.93 ppm), B (3.82–28.99 ppm), Ga (0.39–1.51 ppm), Ge (1.70–5.15 ppm) and As (2.40–10.30 ppm).

The Al vs. Li plot (Fig. 11a) shows positive correlations for all layers. Noteworthy, the data points for quartz (Al/Li 2.3 mean value) falls near the 1:1 Al/Li ratio trend typical of hydrothermal and magmatic quartz (e.g., Dennen 1966; Müller et al. 2018; Rabiee et al. 2019) whereas those for cristobalite (Al/Li 83.9 mean value) and chalcedony–moganite

layers (Al/Li 58.7 mean value, with chalcedony and moganite having Al/Li 43.4 and 82.5 mean values, respectively) are well discriminated by Al/Li ratios higher than the 15:1 trendline. The hydrothermal genetic environment is highlighted also by the Al vs. Ge diagram (Fig. 11b) where the analyses yield invariably Ge contents higher than those expected for magmatic systems (e.g., Jacamon and Larsen 2009; Müller et al. 2018) and typical of hydrothermal environments (e.g., Müller et al. 2018). The few available Ti data confirm the possible hydrothermal genesis (Fig. 11c); moreover, the logarithmic Ti vs. Al diagram (Fig. 11d; after Rusk 2012; Müller et al. 2018; Rabiee et al. 2019) suggests a possible affinity with the conditions of orogenic Au-bearing quartz deposits typically constituted by chalcedony and cryptocrystalline quartz mineralization (e.g., Kogen and Timachev 1969; Klein and Fuzikawa 2010).

Finally, plots in Fig. 11e show that arsenic and boron contents are variable in crystalline quartz and chalcedony–moganite layers. Quartz (layer #11) shows the lowest values for B and As (mean values 16.22 and 6.74 ppm, respectively). Progressively higher values of B and As are obtained for cristobalite (mean values

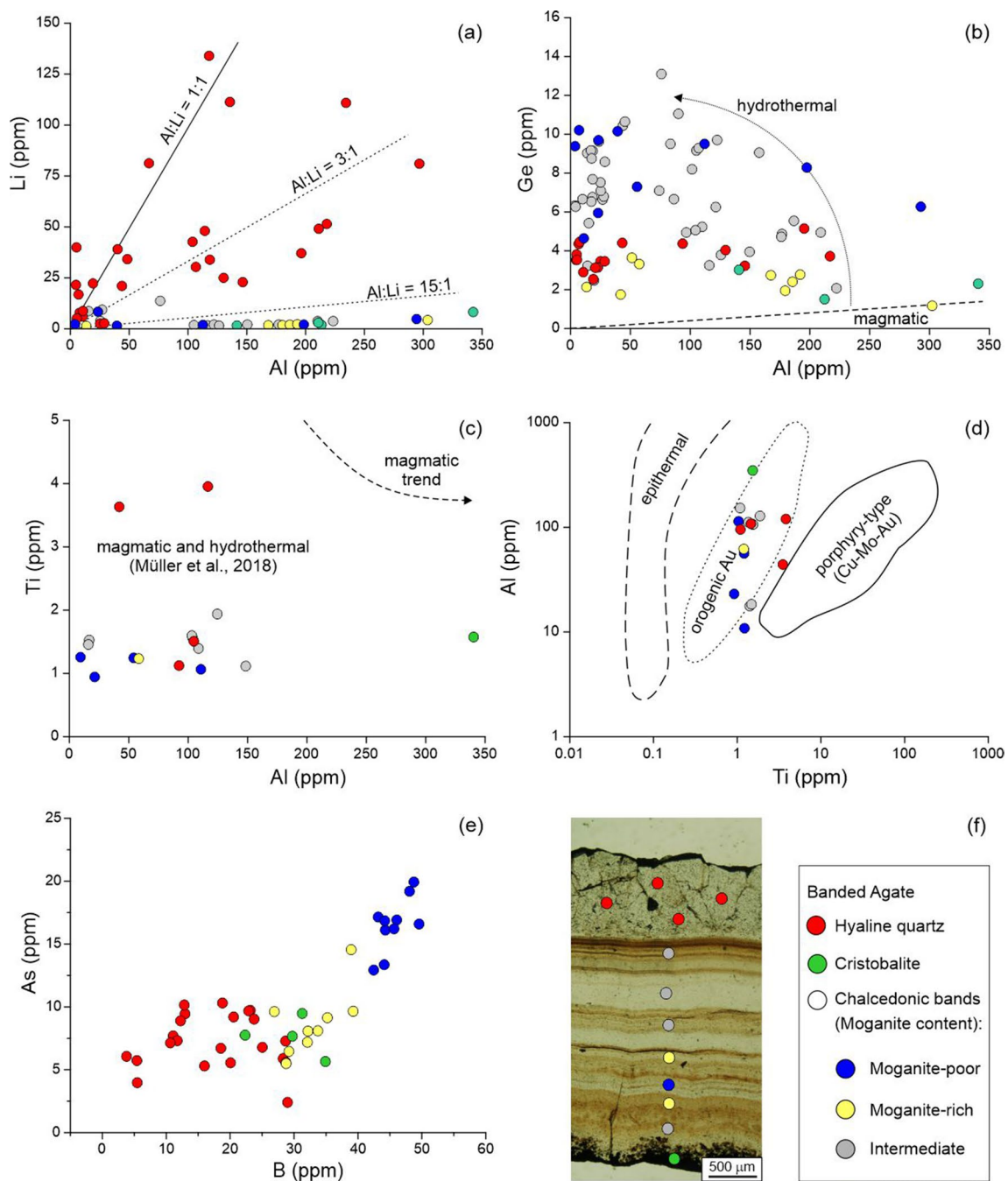


Fig. 11 Trace element chemistry of the banded agate sample. **a–e**, the number of dots varies from a diagram to another because many measurements did not provide reliable data. **e** intermediate moganite content dots were discarded for the sake of clarity

29.57 and 7.63 ppm, respectively) and moganite-rich chalcedony (mean values 32.93 and 8.69 ppm, respectively), whereas highest values are obtained for moganite-poor chalcedony (mean values 45.64 and 8.69 ppm, respectively).

Discussion

The silica growth in the sample studied can be schematically described as: (i) cristobalite forming in the early stages of growth, (ii) an alternating sequence of

chalcedony and moganite-rich bands, and (iii) a final crystallization of euhedral hyaline quartz. This sequence is widely reported in the literature (Lee 2007; Richter et al. 2015; Dumańska-Słowik et al. 2018) and it is generally interpreted as (i) a combination of different flux rates (varying in silica saturation) during the agate growth (Lee 2007; Dumańska-Słowik et al. 2013, 2018; French et al. 2013; Natkaniec-Nowak et al. 2020), or (ii) an oscillatory zonation resulting from a cyclic interplay between growth rate and diffusion rates at a crystal/solution interface (Fron del 1985; Wang and Merino 1990; Howard and Rabinovitch 2018). The observed textural variations in the banded agates studied, together with the occurrence of nucleation layers, seems to suggest a multi-stage growth process.

The genesis of the two varieties (chalcedony-rich vs. moganite-rich) of fibrous silica is interpreted as the response to physicochemical fluctuations of a circulating hydrothermal solution with moganite-rich zones indicative of alkaline and/or sulfate characters of the SiO₂ bearing fluids (Folk and Pittman 1971; Pop et al. 2004; Dumańska-Słowik et al. 2013, 2018; Richter et al. 2015), whereas chalcedony-rich layers are due to more acidic conditions (Qiu et al. 2021) as also supported by their relevant boron- and arsenic-enrichment. More in detail, the observed variations in boron across the layers of our sample are compatible with pH fluctuations of the agate-forming hydrothermal fluids, with boron enrichment associated to moderately to strongly acidic conditions (e.g., Qiu et al. 2021 and references therein).

Noteworthy, this compositional zoning overlaps with water distribution, as revealed by combined Raman and FT-IR single spectra and imaging, revealing an unexpected H₂O-rich character in chalcedony opposite to a H₂O-poor behavior of the moganite-rich bands. According to our spectroscopy data, the anticorrelation occurs not just between moganite content and total water signal (molH₂O + SiOH qualitatively estimated with the integral area of the 2750–3750 cm⁻¹ water band), but also for moganite content with molecular water and silanol signal singularly (qualitatively estimated by integral area of their components extrapolated by the fitting procedure). This anticorrelation is unexpected as the opposite is suggested in the literature (Graetsch et al. 1987, 1994; Schmidt et al. 2013; Moxon 2017). However these studies are performed on several agate samples from different genetic environment, and in particular, the study of Moxon 2017 focuses on agate samples of different ages, revealing that both water and moganite content decrease with time. This suggests that aging may have a strong effect on both the moganite and water contents of the agate. By contrast, our results were obtained within a single sample, across

different layers corresponding to a continuous growing sequence. Moreover our spectroscopy data point to a direct proportion between molecular water and silanol components: this is also in apparent contradiction with literature that argues for a higher SiOH/molH₂O ratio in moganite samples (Miehe and Graetsch 1992; Schmidt et al. 2013). However the study of Miehe and Graetsch (1992) compares pure moganite sample with chalcedony samples of unknown moganite content taken from literature, and both of the studies present data of agates of different ages and genetic environments.

Lastly, the high moganite contents (up to 48%) provides also as thermometry and indication suggesting a growth for T ranging between 100 and 200 °C (Zhang et al. 2020).

Besides the composition of the agate banding, additional micro-textural features can provide insights on the physicochemical genetic conditions. Primary textures observed in the sample such as colloform or botryoidal textures can be interpreted as the result of nucleation and growth processes starting in the innermost portion of a free space (Dong et al. 1995; Götze et al. 2020). The nucleation layers made up of spherical structures is a further evidence of high driving force and low growth rate (Sunagawa 2007). On the contrary, the crystallization of moganite and the presence of mineral inclusions such as Fe-oxides and sulfates during the early and late stages of agate growth could be interpreted as the response of temporarily alkaline-rich fluid compositions and the presence of Fe³⁺, SO₄²⁻ in the SiO₂-bearing hydrothermal solutions (Heaney 1995; Pop et al. 2004; Dumańska-Słowik et al. 2013, 2018; Natkaniec-Nowak et al. 2016). The transition from silica fibers to euhedral quartz crystals represents the last stage of the cavity-filling and can be interpreted as the response to (i) higher temperature solutions entering the cavity, or (ii) modifications of the silica supersaturation degree (Fron del 1978). The latter hypothesis is also in agreement with the crystal-growth process proposed by Heaney and Davis (1995), where the solution is characterized by a sufficiently low silica concentration to allow the slow growth of defect-free and essentially anhydrous quartz crystals. The hydrothermal Bambauer quartz with typical μm-sized growth lamellae indicates a lower temperature of hydrothermal fluids characterized by strong fluctuations in silica concentrations and/or pH conditions (Bambauer et al. 1961; Richter et al. 2015; Powolny et al. 2019; Götze et al. 2020; Pršek et al. 2020) or episodic crystallization, with periods of stasis alternating with periods of growth. Lastly the local evidence of feathery/splintery extinction of some quartz crystals agrees with subsequent recrystallization of metastable silica phases such as chalcedony or amorphous silica (Fournier 1985; Yilmaz et al. 2016; Powolny et al. 2019; Götze et al. 2020; Pršek et al. 2020).

Conclusion

An integration of mineralogical and spectroscopic data show that the banded agates from the Tolfa volcanic complex are the result of a complex multi-stage genetic process triggered by the late-magmatic hydrothermal SiO₂-bearing fluids. These fluids are characterized by variably acidic to alkaline- and/or sulfate-rich compositions and physicochemical conditions, with temperatures in the range 100–200 °C. Obtained results agree with the few existing literature exploring the genetic scenario of the Allumiere-Tolfa ore basin characterized by hydrothermal/metasomatic processes at low-depth due to late-magmatic hydrothermal fluids at T 120–140 ± 25 °C (from oxygen isotope data in Lombardi and Sheppard 1977), which produced an extensive alteration of the pre-existing rocks with consequent formation of the sulfates (alunite group) + kaolinite + silica paragenesis (Lombardi and Sheppard 1977). This mineral assemblage was indicated by Hedenquist et al. (2000) to be typical of the “silicic” to “advanced argillic” alteration zones characterized by a depth of 0–150 m and a temperature ranging from 100 to 200 °C and capping the deeper potassic and sodic-calcic alteration zones (e.g., Lucci et al. 2018) of an epithermal ore deposit.

The fluid-driven hydrothermal genetic environment for the studied sample is also well highlighted by the LA-ICP-MS trace element chemistry (Fig. 11; see also Rabiee et al. 2019). It is worth noting that the positive correlation between Al and Li in the hyaline quartz (and chalcedony) from the investigated sample. Similar relationship has been reported by i.e., Yilmaz et al. (2016) or Perny et al. (1992) and can be attributed to Si ↔ Al(+Li) substitution in the crystal lattice during the crystal growth in hydrothermal environment. Moreover, according to this author, the presence of feathery quartz may also account for variable amounts of Al and Li in hydrothermal quartz. Low Ti contents in the investigated sample suggest that the agate-forming fluids were likely below 300 °C (Gotte et al., 2012), which stays in agreement with the mineralogical and micro-textural observations (i.e., high moganite content), as well as previous studies focused on the agate formation temperatures (please add one or more references, there are some papers consisting O isotope study as a proxy for agate formation temperatures). Furthermore, variations in As and B (i.e., enrichment in chalcedony-rich relative to quartz-rich and moganite-rich layers—see Fig. 11e, f) can be ascribed to fluctuations (i.e., alkaline-acidic) of agate-forming fluids and/or crystallization of silica from either H₂O vapor or H₂O liquid phase (Harris 1989).

Coupled Raman and FT-IR investigation across the growing sequence of the agate sample reveals an anticorrelation between moganite and water (molH₂O + SiOH) signal which

is apparently contrasting with literature data (Graetsch et al. 1987, 1994; Schmidt et al. 2013; Moxon 2017). Moreover, our spectroscopy data point to a coevolution of the molecular water and silanol components, also in apparent contrast with literature (Miehe and Graetsch 1992; Schmidt et al. 2013). However, it has to be noted that literature data refer to different agate samples of different ages and genetic environment while our study focuses on the relative content of moganite and water across the layers of a single sample.

Supplementary Information The online version contains supplementary material available at <https://doi.org/10.1007/s00269-022-01214-5>.

Acknowledgements The constructive reviews of Tomasz Powolny and Peter Heaney as well the professional handling of the Editor Larissa Dobrzhinetskaya greatly contributed to improve the manuscript. The authors thank the DAFNE Light Technical staff for the technical support during the analytical sessions. The Grant to Department of Science, Roma Tre University (MIUR-Italy Dipartimenti di Eccellenza, ARTICOLO 958 1, COMMI 314-337 LEGGE 232/2016) is gratefully acknowledged. Thanks are due Dario di Domenico for providing some of the studied samples. The authors wish to greatly thank Laurent Lenta (Laboratoire de Planétologie et Géosciences, Université de Nantes) for sample preparation.

Author contributions AC, GDV and FL conceptualized the work. AC, GDV, FL and CN carried out the field work and the petrographic investigation. AC, BR GDV, MR and MCG were responsible for SEM, Raman and FT-IR investigations. FL, AC and CL were responsible for in situ LA-ICP-MS investigation and data discussion. AC, BR and GDV wrote the early version of the manuscript. All authors revised the manuscript and approved the final version.

Funding Open access funding provided by Università degli Studi Roma Tre within the CRUI-CARE Agreement. Financial support by the Grant to Department of Science, Roma Tre University (MIUR-Italy Dipartimenti di Eccellenza, ARTICOLO 1, COMMI 314-337 LEGGE 232/2016) is gratefully acknowledged.

Declarations

Conflict of interest The authors declare that they have no known competing financial interests or personal relationships that could have appeared to influence the work reported in this paper.

Open Access This article is licensed under a Creative Commons Attribution 4.0 International License, which permits use, sharing, adaptation, distribution and reproduction in any medium or format, as long as you give appropriate credit to the original author(s) and the source, provide a link to the Creative Commons licence, and indicate if changes were made. The images or other third party material in this article are included in the article's Creative Commons licence, unless indicated otherwise in a credit line to the material. If material is not included in the article's Creative Commons licence and your intended use is not permitted by statutory regulation or exceeds the permitted use, you will need to obtain permission directly from the copyright holder. To view a copy of this licence, visit <http://creativecommons.org/licenses/by/4.0/>.

References

- Aines RD, Rossman GR (1984) Water in minerals? A peak in the infrared. *J Geophys Res Solid Earth* 89(B6):4059–4071
- Anedda A, Carbonaro CM, Clemente F, Corpino R, Grandi S, Mustarelli P, Magistris A (2003) OH-dependence of ultraviolet emission in porous silica. *J Non-Cryst Solids* 322(1–3):68–72
- Awadh SM, Yaseen ZM (2019) Investigation of silica polymorphs stratified in siliceous geode using FTIR and XRD methods. *Mater Chem Phys* 228:45–50
- Bambauer HU, Brunner GO, Laves F (1961) Beobachtungen über Lamellenbau an Bergkristallen I. *Z Kristallogr* 116(3–6):173–181
- Bates JB (1972) Raman spectra of α and β cristobalite. *J Chem Phys* 57(9):4042–4047
- Behl RJ (1999) The monterey formation: the source of oil. Geological Society of America, Boulder
- Berenblut BJ, Dawson P, Wilkinson GR (1973) A comparison of the Raman spectra of anhydrite (CaSO_4) and gypsum ($\text{CaSO}_4 \cdot 2\text{H}_2\text{O}$). *Spectrochim Acta A Mol Spectrosc* 29(1):29–36
- Boboň M, Christy AA, Kluvanec D (2011) State of water molecules and silanol groups in opal minerals: a near infrared spectroscopic study of opals from Slovakia. *Phys Chem Miner* 38(10):809–818
- Bustillo MA, Pérez-Jiménez JL, Alonso-Zarza AM, Furio M (2012) Moganite in the chalcidony varieties of continental cherts (Miocene, Madrid Basin, Spain). *Spectrosc Lett* 45:109–113
- Cady SL, Wenk HR, Sintubin M (1998) Microfibrous quartz varieties: characterization by quantitative X-ray texture analysis and transmission electron microscopy. *Contrib Mineral Petrol* 130(3):320–335
- Calderoni G, Ferrini V, Masi U (1985) Distribution and significance of Pb and Tl in the sulfides and host rocks from the hydrothermal mineralization of the Tolfa Mountains (Latium, Central Italy). *Chem Geol* 51(1–2):29–39
- Chauviré B, Rondeau B, Mangold N (2017) Near infrared signature of opal and chalcidony as a proxy for their structure and formation conditions. *Eur J Mineral* 29(3):409–421
- Chauviré B, Thomas PS (2020) DSC of natural opal: insights into the incorporation of crystallizable water in the opal microstructure. *J Therm Anal Calorim* 140(5):2077–2085
- Cimarelli C, De Rita D (2006) Relatively rapid emplacement of dome-forming magma inferred from strain analyses: The case of the acid Latian dome complexes (Central Italy). *J Volcanol Geotherm Res* 158(1–2):106–116
- Curtis NJ, Gascooke JR, Johnston MR, Pring A (2019) A review of the classification of opal with reference to recent new localities. *Minerals* 9(5):299
- Davis KM, Tomozawa M (1996) An infrared spectroscopic study of water-related species in silica glasses. *J Non-Cryst Solids* 201(3):177–198
- Day R, Jones B (2008) Variations in water content in opal-A and opal-CT from geyser discharge aprons. *J Sediment Res* 78(4):301–315
- Della Ventura G, Marcelli A, Bellatreccia F (2014) SR-FTIR microscopy and FTIR imaging in the Earth Sciences. *Rev Mineral Geochim* 78(1):447–479
- Della Ventura G, Patanè A (2020) Le miniere dei Monti della Tolfa-Allumiere. *Memorie Descrittive Della Carta Geologica D'italia* 106:23–32
- De Rita D, Bertagnini A, Faccenna C, Landi P, Rosa C, Zarlenga F, Di Filippo M, Carboni G (1997) Evoluzione geopetrografica-strutturale dell'area tolfetana. *Bollettino Della Società Geologica Italiana* 116(1):143–175
- Dennen WH (1966) Stoichiometric substitution in natural quartz. *Geochim Cosmochim Acta* 30(12):1235–1241
- Dong G, Morrison G, Jaireth S (1995) Quartz textures in epithermal veins, Queensland; classification, origin and implication. *Econ Geol* 90(6):1841–1856
- Dumańska-Słowik M, Natkaniec-Nowak L, Weselucha-Birczynska A, Gaweł A, Lankosz M, Wróbel P (2013) Agates from Morocco: gemological characteristics and proposed origin. *Gems Gemol* 49(3):148–159
- Dumańska-Słowik M, Powolny T, Sikorska-Jaworowska M, Gaweł A, Kogut L, Poloński K (2018) Characteristics and origin of agates from Płóczki Górne (Lower Silesia, Poland): a combined microscopic, micro-Raman, and cathodoluminescence study. *Spectrochim Acta A Mol Biomol Spectrosc* 192:6–15
- Eckert J, Gourdon O, Jacob DE, Meral C, Monteiro PJ, Vogel SC, Wirth R, Vogel SC, Wenk HR (2015) Ordering of water in opals with different microstructures. *Eur J Mineral* 27(2):203–213
- Elzea JM, Rice SB (1996) TEM and X-ray diffraction evidence for cristobalite and tridymite stacking sequences in opal. *Clays Clay Miner* 44(4):492–500
- Fazzini P, Gelmini R, Mantovani MP, Pellegrini M. (1972) *Geologia dei monti della Tolfa*. (Lazio settentrionale; province di Viterbo e Roma)
- Ferrini V, Lombardi G, Morbidelli L, Negretti G. (1975) *Studio geopetrografico del complesso vulcanico tolfetano-cerite (Lazio)*. VII b. Le mineralizzazioni a solfuri misti in un settore dei Monti della Tolfa: Università di Roma, Centro Studi CNR. Istituto di Petrografia, Roma, 63
- Flörke OW, Jones JB, Schmincke HU (1976) A new microcrystalline silica from Gran Canaria. *Zeitschrift Für Kristallographie-Crystalline Materials* 143(1–6):156–165
- Flörke OW, Köhler-Herbertz B, Langer K, Tönges I (1982) Water in microcrystalline quartz of volcanic origin: agates. *Contrib Mineral Petrol* 80(4):324–333
- Flörke OW, Flörke U, Giese U (1984) Moganite: a new microcrystalline silica-mineral. *Neues Jahrbuch Für Mineralogie* 149:325–336
- Flörke OW, Graetsch H, Martin B, Röller K, Wirth R (1991) Nomenclature of micro- and non-crystalline silica minerals, based on structure and microstructure. *Neues Jahrbuch Für Mineralogie* 163(1):19–42
- Folk RL, Pittman JS (1971) Length-slow chalcidony; a new testament for vanished evaporites. *J Sediment Res* 41(4):1045–1058
- Fournier RO. (1985) The behavior of silica in hydrothermal solutions
- French MW, Worden RH, Lee DR (2013) Electron backscatter diffraction investigation of length-fast chalcidony in agate: implications for agate genesis and growth mechanisms. *Geofluids* 13(1):32–44
- Frondel C (1978) Characters of Quartz Fibers *Am Mineral* 63(1–2):17–27
- Frondel C (1985) Systematic compositional zoning in the quartz fibers of agates. *Am Mineral* 70(9–10):975–979
- Götte T, Ramseyer K (2012) Trace element characteristics, luminescence properties and real structure of quartz. *Quartz: deposits, mineralogy and analytics*. Springer, Berlin, pp 265–285
- Götze J, Nasdala L, Kleeberg R, Wenzel M (1998) Occurrence and distribution of “moganite” in agate/chalcidony: a combined micro-Raman, Rietveld, and cathodoluminescence study. *Contrib Mineral Petrol* 133(1):96–105
- Götze J, Plötze M, Tichomirowa M, Fuchs H, Pilot J (2001) Aluminium in quartz as an indicator of the temperature of formation of agate. *Mineral Mag* 65(3):407–413
- Götze J, Möckel R, Kempe U, Kapitonov I, Vennemann T (2009) Characteristics and origin of agates in sedimentary rocks from the Dryhead area, Montana, USA. *Mineral Mag* 73(4):673–690
- Götze J, Möckel R, Pan Y (2020) Mineralogy, geochemistry and genesis of agate—a review. *Minerals* 10(11):1037
- Götze J, Stanek K, Orozco G, Liesegang M, Mohr-Westheide T (2021) Occurrence and distribution of moganite and Opal-CT in

- agates from Paleocene/Eocene tuffs, El Picado (Cuba). *Minerals* 11(5):531
- Graetsch H, Flörke OW, Miede G (1985) The nature of water in chalcedony and opal-C from Brazilian agate geodes. *Phys Chem Miner* 12(5):300–306
- Graetsch H, Flörke OW, Miede G (1987) Structural defects in microcrystalline silica. *Phys Chem Miner* 14(3):249–257
- Graetsch H, Topalovic I, Gies H (1994) NMR spectra of moganite and chalcedony. *Eur J Mineral* 6(4):459–464
- Harris C (1989) Oxygen-isotope zonation of agates from Karoo volcanics of the Skeleton Coast. *Namibia Am Min* 74(3–4):476–481
- Heaney PJ, Post JE (1992) The widespread distribution of a novel silica polymorph in microcrystalline quartz varieties. *Science* 255(5043):441–443
- Heaney PJ, Sheppard RA, Post JE. (1992) Association of length-slow silica with evaporites. *Geol Soc of America, Abstracts with Programs (United States)*, 24(CONF-921058)
- Heaney PJ (1993) A proposed mechanism for the growth of chalcedony. *Contrib Mineral Petrol* 115(1):66–74
- Heaney PJ (1995) Moganite as an indicator for vanished evaporites; a testament reborn? *J Sediment Res* 65(4a):633–638
- Heaney PJ, Davis AM (1995) Observation and origin of self-organized textures in agates. *Science* 269(5230):1562–1565
- Hedenquist JW, Arribas A, Gonzalez-Urrien E (2000) Exploration for epithermal gold deposits. *SEG Reviews* 13:245–277
- Howard CB, Rabinovitch A (2018) A new model of agate geode formation based on a combination of morphological features and silica sol–gel experiments. *Eur J Mineral* 30(1):97–106
- Iler KR. (1979) The chemistry of silica. Solubility, polymerization, colloid and surface properties and biochemistry of silica
- Jacamon F, Larsen RB (2009) Trace element evolution of quartz in the charnockitic Kleivan granite, SW-Norway: The Ge/Ti ratio of quartz as an index of igneous differentiation. *Lithos* 107(3–4):281–291
- Jochum KP, Weis U, Stoll B, Kuzmin D, Yang Q, Raczek I, Jacob DE, Stracke A, Birbaum K, Frick DA (2011) Determination of reference values for NIST SRM 610–617 glasses following ISO guidelines. *Geostand Geoanalytical Res* 35:397–429
- Jones JT, Segnit ER (1971) The nature of opal I nomenclature and constituent phases. *J Geol Soc Aust* 18(1):57–68
- Kastner M (1980) Length-slow chalcedony: the end of the new testament. *Eos* 61(17):399
- Keene JB (1983) Chalcedonic quartz and occurrence of quartzine (length-slow chalcedony) in pelagic sediments. *Sedimentology* 30(3):449–454
- Klein EL, Fuzikawa K (2010) Origin of the CO₂-only fluid inclusions in the Palaeoproterozoic Carará vein-quartz gold deposit, Ipitinga Auriferous District, SE-Guiana Shield, Brazil: Implications for orogenic gold mineralisation. *Ore Geol Rev* 37(1):31–40
- Knauth LP (1994) Petrogenesis of Chert *Rev Mineral Geochem* 29(1):233–258
- Kogen VS, Timachev VM (1969) Chalcedony-barite auriferous veins in Apsakan District. *Int Geol Rev* 11(6):683–684
- Langer K, Flörke OW (1974) Near infrared absorption spectra (4000–9000 cm⁻¹) of opals and the role of “water” in these SiO₂·nH₂O minerals. *Fortschr Miner* 52(1):17–51
- Lauro C, Negretti GC, Morbidelli L, Lombardi G. (1965) “Studio geopetrografico del complesso vulcanico tolfetano-cerite (Lazio). I. Lineamenti geostrutturali della Tuscia Romana centro-occidentale, con particolare riguardo alle regioni tolfetana, cerite e manziate, e notizie bibliografiche. *Ist Petrogr Univ Roma* 53
- Lee DR. (2007) Characterisation of silica minerals in a banded agate: implications for agate genesis and growth mechanisms. *Masters Res* 1–18
- Lombardi G, Morbidelli L, Negretti GC (1965a) Lineamenti geopetrografici e strutturali degli affioramenti vulcanici del settore Tolfetano (Lazio). *Rendiconti Della Società Mineralogica Italiana A* 21:151–156
- Lombardi G, Morbidelli L, Negretti GC (1965b) Gli affioramenti eruttivi della Tolfaccia (Monti della Tolfa). *Rendiconti Della Società Mineralogica Italiana* 21:157–164
- Lombardi G, Nicoletti M, Petrucciani C (1974) Età delle vulcaniti acide del complesso Tolfetano Cerite e Manziate (Lazio nordoccidentale). *Period Di Mineral* 43:351–376
- Lombardi G, Sheppard SMF (1977) Petrographic and isotopic studies of the altered acid volcanics of the Tolfa-Cerite area, Italy: the genesis of the clays. *Clay Miner* 12(2):147–162
- Lucci F, Della Ventura G, Conte A, Nazzari M, Scarlato P (2018) Naturally occurring asbestos (NOA) in granitoid rocks, a case study from Sardinia (Italy). *Minerals* 8(10):442
- Marinelli G (1961) Genesi e classificazione delle vulcaniti recenti toscane. *Atti Società Toscana Di Scienze Naturali Pisa Memorie Serie A* 68:63–116
- Masi U, Ferrini V, O’Neil JR, Batchelder JN (1980) Stable isotope and fluid inclusion studies of carbonate deposits from the Tolfa Mountains Mining district (Latium, Central Italy). *Miner Deposita* 15(3):351–359
- Merino E, Wang Y, Delouie E (1995) Genesis of agates in flood basalts; twisting of chalcedony fibers and trace-element geochemistry. *Am J Sci* 295(9):1156–1176
- Michel-Lévy A, Munier-Chalmas E (1892) Mémoire sur diverses formes affectées par le réseau élémentaire du quartz. *Bull Minér* 15(7):159–190
- Miede G, Graetsch H, Flörke OW (1984) Crystal structure and growth fabric of length-fast chalcedony. *Phys Chem Miner* 10(5):197–199
- Miede G, Graetsch H (1992) Crystal structure of moganite: a new structure type for silica. *Eur J Mineral* 4(4):693–706
- Moxon T, Lee M (2017) A re-examination of water in agate and its bearing on the agate genesis enigma. *Mineral Mag* 81(5):1223–1244
- Moxon T, Palyanova G (2020) Agate genesis: a continuing enigma. *Minerals* 10(11):953
- Müller A, Herklotz G, Giegling H (2018) Chemistry of quartz related to the Zinnwald/Cinovec Sn-W-Li greisen-type deposit, Eastern Erzgebirge, Germany. *J Geochem Explor* 190:357–373
- Natkaniec-Nowak L, Dumańska-Słowik M, Pršek J, Lankosz M, Wróbel P, Gawel A, Kowalczyk J, Kocemba J (2016) Agates from Kerrouchen (the Atlas mountains, Morocco): textural types and their gemmological characteristics. *Minerals* 6(3):77
- Natkaniec-Nowak L, Dumańska-Słowik M, Gawel A, Łatkiewicz A, Kowalczyk-Szpyt J, Wolska A, Milovská S, Luptáková J, Ładoń K (2020) Fire agate from the deer creek deposit (Arizona, USA)—new insights into structure and mineralogy. *Mineral Mag* 84(2):343–354
- Negretti GC, Lombardi G, Morbidelli L (1966) Le manifestazioni vulcaniche del settore civitavecchiese-tolfetano. *Università degli Studi di Roma, Centro di studi del C.N.R.*
- Palyanova G, Sidorov E, Borovikov A, Seryotkin Y (2020) Copper-containing agates of the Avacha bay (Eastern Kamchatka, Russia). *Minerals* 10(12):1124
- Perny B, Eberhardt P, Ramseyer K, Mullis J, Pankrath R (1992) Microdistribution of Al, Li, and Na in α quartz: possible causes and correlation with short-lived cathodoluminescence. *Am Min* 77(5–6):534–544
- Pop D, Constantina C, Tatar D, Kiefer W (2004) Raman spectroscopy on gem-quality microcrystalline and amorphous silica varieties from Romania. *Studia UBB Geologia* 49(1):41–52
- Powolny T, Dumańska-Słowik M, Sikorska-Jaworowska M, Wójcik-Bania M (2019) Agate mineralization in spilitized Permian volcanics from “Borówno” quarry (Lower Silesia,

- Poland)—microtextural, mineralogical, and geochemical constraints. *Ore Geol Rev* 114:103130
- Pršek J, Dumańska-Słowik M, Powolny T, Natkaniec-Nowak L, Tobała T, Zych D, Skrepnicka D (2020) Agates from Western Atlas (Morocco)—Constraints from mineralogical and microtextural characteristics. *Minerals* 10(2):198
- Qiu Y, Zhang R, Chou IM, Wang X, Hu W, Zhang W, Jianjun L, Guanglai L, Li Z (2021) Boron-rich ore-forming fluids in hydrothermal W-Sn deposits from South China: Insights from in situ Raman spectroscopic characterization of fluid inclusions. *Ore Geol Rev* 132:104048
- Rabiee A, Rossetti F, Tecce F, Asahara Y, Azizi H, Głodny J, Lucci F, Nozaem R, Opitz J, Selby D (2019) Multiphase magma intrusion, ore-enhancement and hydrothermal carbonatisation in the Siah-Kamar porphyry Mo deposit, Urumieh-Dokhtar magmatic zone. *NW Iran Ore Geol Rev* 110:102930
- Richter S, Götze J, Niemeyer H, Möckel R (2015) Mineralogical investigations of agates from Cordón de Lila. *Chile Andean Geol* 42(3):386–396
- Rondeau B, Cenki-Tok B, Fritsch E, Mazzero F, Gauthier JP, Bodeur Y, Bekele E, Gaillou E, Ayalew D (2012) Geochemical and petrological characterization of gem opals from Wegel Tena, Wollo, Ethiopia: opal formation in an Oligocene soil. *Geochem: Explor Environ Anal* 12(2):93–104
- Rusk B (2012) Cathodoluminescent textures and trace elements in hydrothermal quartz. In: Götze J, Möckel R (eds) *Quartz: deposits mineralogy and analytics*. Springer, Heidelberg New York, pp 307–329
- Serri G, Innocenti F, Manetti P (1993) Geochemical and petrological evidence of the subduction of delaminated adriatic continental lithosphere in the genesis of the neogene-quadernary magmatism of central Italy. *Tectonophysics* 223(1–2):117–147
- Schmidt P, Slodczyk A, Léa V, Davidson A, Puaud S, Sciau P (2013) A comparative study of the thermal behaviour of length-fast chalcedony, length-slow chalcedony (quartzine) and moganite. *Phys Chem Miner* 40(4):331–340
- Sodo A, Casanova Municchia A, Barucca S, Bellatreccia F, Della Ventura G, Butini F, Ricci MA (2016) Raman, FT-IR and XRD investigation of natural opals. *J Raman Spectrosc* 47(12):1444–1451
- Sunagawa I (2007) *Crystals: growth, morphology, & perfection*. Cambridge University Press, Cambridge
- Taylor HP, Turi B (1976) High-¹⁸⁰ igneous rocks from the Tuscan magmatic province. *Italy Contrib Mineral Petrol* 55(1):33–54
- Thomas P, Šesták J, Heide K, Fueglein E, Šimon P (2010) Thermal properties of Australian sedimentary opals and Czech moldavites. *J Therm Anal Calorim* 99(3):861–867
- Vollmer R (1977) Isotopic evidence for genetic relations between acid and alkaline rocks in Italy. *Contrib Mineral Petrol* 60(2):109–118
- Wang Y, Merino E (1990) Self-organizational origin of agates: banding, fiber twisting, composition, and dynamic crystallization model. *Geochim Cosmochim Acta* 54(6):1627–1638
- Yilmaz TI, Duschl F, Di Genova D (2016) Feathery and network-like filamentous textures as indicators for the re-crystallization of quartz from a metastable silica precursor at the Rusey Fault Zone, Cornwall. *UK Solid Earth* 7(6):1509–1519
- Zhang X, Ji L, He X (2020) Gemological characteristics and origin of the Zhanguohong agate from Beipiao, Liaoning province, China: a combined microscopic, X-ray diffraction, and Raman spectroscopic study. *Minerals* 10(5):401

Publisher's Note Springer Nature remains neutral with regard to jurisdictional claims in published maps and institutional affiliations.